

3

Free surface flows that intersect walls

We continue our study of free surface flows by considering the two-dimensional flow shown in Figure 3.1. The flow domain is bounded below by the horizontal wall AB and above by the inclined walls CD and DE and the free surface EF . The fluid is assumed to be incompressible and inviscid and the flow is assumed to be irrotational and steady. We introduce cartesian coordinates with the x -axis along the horizontal wall AB and the y -axis through the separation point E (here a separation point refers to an intersection of a free surface and a rigid wall). The angles between the walls CD and DE and the horizontal are denoted by γ_1 and γ_2 respectively.

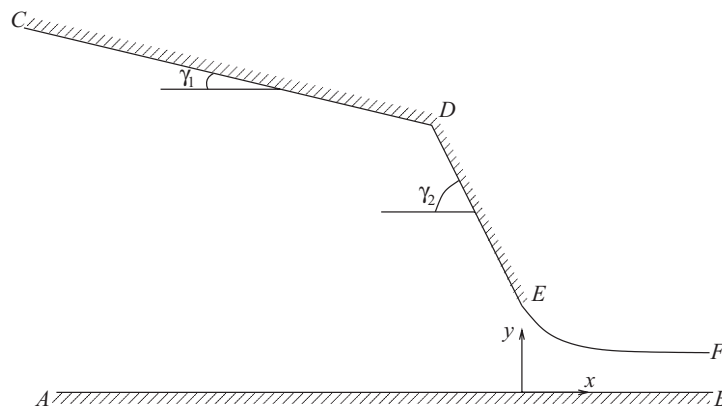


Fig. 3.1. A two-dimensional free surface flow bounded by the walls CD , DE and AB and the free surface EF . The separation point E is defined as the point at which the free surface EF meets the wall DE . The flow is from left to right.

The configuration of Figure 3.1 was chosen because it can be used to describe many properties of free surface flows that intersect, i.e. adjoin,

rigid walls. These properties when understood for the flow of Figure 3.1 can then be used to describe locally flows with more complex geometries.

There are various illustrations of the flow of Figure 3.1. The first is the flow emerging from a container bounded by the walls CD , DE and AB . When $\gamma_1 = \gamma_2 = \pi/2$, the configuration of Figure 3.1 models the flow under an infinitely high gate (see Figure 3.2). Here the point D is irrelevant and has been omitted from the figure.

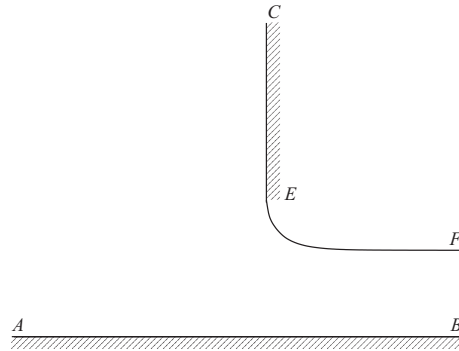


Fig. 3.2. The free surface flow under a gate. The flow is from left to right, and the labels C , A , F and B indicate points at an infinite distance from E .

When $\gamma_1 = 0$ and $\gamma_2 < 0$, Figure 3.1 describes locally the flow near the bow or the stern of a ship (see Figure 3.3). A clear distinction between the stern and bow flows will be introduced in Chapter 8, when we discuss gravity flows with a train of waves in the far field. Further particular cases of Figure 3.1, which model bubbles rising in a fluid and jets falling from a nozzle, are described in Section 3.3.2.

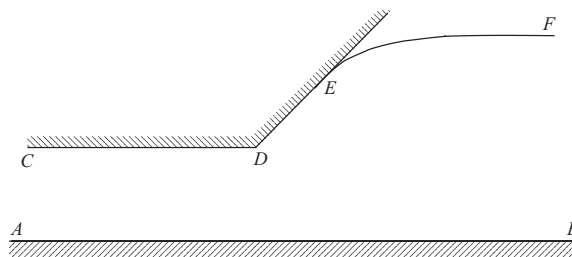


Fig. 3.3. A model for the free surface flow near the bow or stern of a ship.

As mentioned in Chapter 1 we will proceed with problems of increasing complexity. Section 3.1 is devoted to free surface flows with $g = 0$ and

$T = 0$. Such flows are called free streamline flows and the corresponding free surfaces are called free streamlines. In Section 3.2 we will study the effect of surface tension ($T \neq 0, g = 0$). In Section 3.3 we will examine the effect of gravity ($T = 0, g \neq 0$). The combined effects of gravity and surface tension ($T \neq 0, g \neq 0$) are considered in Section 3.4.

3.1 Free streamline solutions

3.1.1 Forced separation

We consider the flow configuration of Figure 3.1. Here the effects of gravity and surface tension will be neglected ($T = 0, g = 0$). We refer to this problem as one of forced separation because the free surface is ‘forced’ to separate at the point E where the wall DE terminates. We denote by u and v the horizontal and vertical components of the velocity. Using the incompressibility of the fluid and the irrotationality of the flow, we define a potential function $\phi(x, y)$ and a streamfunction $\psi(x, y)$. As shown in Section 2.3, the complex potential $f = \phi + i\psi$ and the complex velocity $w = u - iv = df/dz$ are both analytic functions of $z = x + iy$.

The wall AB is a streamline along which we choose $\psi = 0$. The walls CD and DE and the free surface EF define another streamline, along which the constant value of ψ is denoted by Q . We also choose $\phi = 0$ at the separation point E . These two choices ($\psi = 0$ on AB and $\phi = 0$ at E) can be made without loss of generality because ϕ and ψ are defined up to arbitrary additive constants. Bernoulli’s equation (2.13) with $\Omega = 0$ yields

$$\frac{1}{2}(u^2 + v^2) + \frac{p}{\rho} = \text{constant} \quad (3.1)$$

everywhere in the fluid. The free surface EF separates the fluid from the atmosphere which is assumed to be characterised by a constant pressure p_a . In the absence of surface tension, which we are assuming, the pressure is continuous across the free surface (see (2.19)). Therefore $p = p_a$ on the free surface. It follows from (3.1) that

$$u^2 + v^2 = U^2 \quad \text{on} \quad EF, \quad (3.2)$$

where U is a constant.

A significant simplification in the formulation of the problem is obtained by using ϕ and ψ as independent variables. This choice was used by Stokes [144], to study gravity waves, and by Helmholtz [71] and Kirchhoff [90] (see also [19] and [69]) to investigate free streamline flows. We shall use it extensively in our studies of gravity–capillary free surface flows. The

simplification comes from the fact that the flow domain is mapped into the strip $0 < \psi < Q$ shown in Figure 3.4. The free surface EF (whose position was unknown in the physical plane $z = x + iy$ of Figure 3.1) is now part of the known boundary $\psi = Q$ in the f -plane. Since $u - iv$ is an analytic function of z and z is an analytic function of f (the inverse of an analytic function is also an analytic function), $u - iv$ is an analytic function of f .

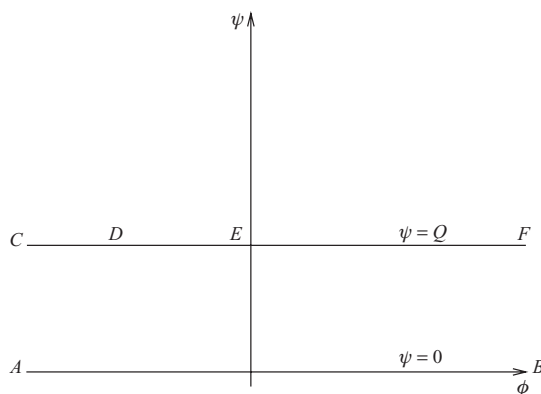


Fig. 3.4. The flow configuration of Figure 3.1 in the complex potential plane $f = \phi + i\psi$.

A remarkable result is that many free streamline problems can be solved in closed form (see Birkhoff and Zarantonello [19] and Gurevich [69]). These exact solutions are obtained by using conformal mappings, and several methods have been derived to calculate them. The method we now choose to describe uses a mapping of the flow domain into the unit circle. It was chosen because it yields naturally to the series truncation methods used in Sections 3.2–3.4 to solve numerically problems with gravity and surface tension included.

In the absence of gravity and surface tension, the flow approaches a uniform stream of constant depth H as $x \rightarrow \infty$. It follows from the dynamic boundary condition (3.2) that this uniform stream is characterised by a constant velocity U . Since $\psi = 0$ on AB and $\psi = Q$ on EF , $H = Q/U$.

We define the logarithmic hodograph variable $\tau - i\theta$ by the relation

$$w = u - iv = e^{\tau - i\theta}. \quad (3.3)$$

The function $\tau - i\theta$ has some interesting properties. First, the quantity $\tau = \frac{1}{2} \ln(u^2 + v^2)$ is constant along free streamlines (see (3.2)). Second, θ can be interpreted as the angle between the vector velocity and the horizontal.

Third, (3.3) leads, for steady flows, to a very simple formula for the curvature of a streamline. This formula can be derived as follows. Since the vector velocity is tangent to streamlines, θ is the angle between the tangent to a streamline and the horizontal. The curvature K of a streamline is given by (2.45). Using the chain rule, we can rewrite (2.45) as

$$K = -\frac{\partial\theta}{\partial\phi} \frac{\partial\phi}{\partial s} - \frac{\partial\theta}{\partial\psi} \frac{\partial\psi}{\partial s}. \quad (3.4)$$

Along a streamline ψ is constant and therefore

$$\frac{\partial\psi}{\partial s} = 0 \quad \text{and} \quad \frac{\partial\phi}{\partial s} = e^\tau. \quad (3.5)$$

Substituting (3.5) into (3.4) yields the simple formula

$$K = -e^\tau \frac{\partial\theta}{\partial\phi}. \quad (3.6)$$

We now introduce dimensionless variables by using U as the reference velocity and H as the reference length. Therefore $\psi = 1$ on the walls CD and DE and on the free surface EF . The dynamic boundary condition (3.2) becomes

$$u^2 + v^2 = 1 \quad \text{on} \quad EF. \quad (3.7)$$

We map the strip $ABFC$ shown in Figure 3.4 into the unit circle in the t -plane by the conformal mapping

$$e^{-\pi f} = \frac{(1-t)^2}{4t}. \quad (3.8)$$

The flow configuration in the t -plane is shown in Figure 3.5. It can easily be checked that the points A and C are mapped into $t = 0$ and the points B and F are mapped into $t = 1$. The value of t at the point D is d . The free surface EF is mapped onto the portion

$$t = e^{i\sigma}, \quad 0 < \sigma < \pi, \quad (3.9)$$

of the unit circle. This can easily be shown by noting that the substitution of (3.9) into (3.8) gives, after some algebra,

$$\phi = -\frac{1}{\pi} \ln \sin^2 \frac{\sigma}{2} \quad \text{on} \quad \psi = 1. \quad (3.10)$$

As σ varies from 0 to π , ϕ varies from ∞ to 0, so that (3.9) is the image of the free surface in the t -plane.

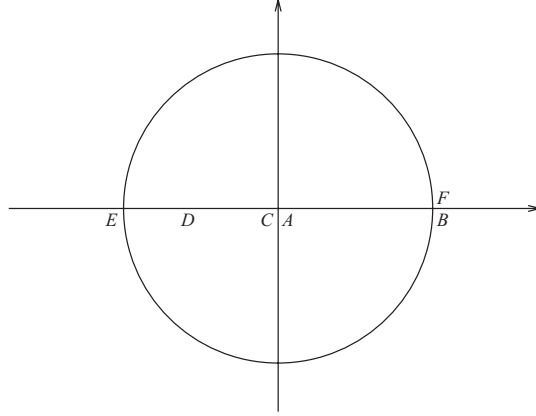


Fig. 3.5. The flow configuration of Figure 3.1 in the complex t -plane.

One might attempt to represent the complex velocity $w = u - iv$ by the series

$$w = \sum_{n=0}^{\infty} a_n t^n. \quad (3.11)$$

However, the series will not converge inside the unit circle $|t| \leq 1$, because singularities can be expected at the corner D and as $x \rightarrow -\infty$ (i.e. at $t = 0$). Nevertheless we can generalise the representation (3.11) by writing

$$w = G(t) \sum_{n=0}^{\infty} a_n t^n, \quad (3.12)$$

where the function $G(t)$ contains all the singularities of w . As we shall see in Sections 3.2–3.4, this type of series representation enables the accurate calculation of many free surface flows with gravity and surface tension included. For the present problem we require $G(t)$ to behave like w as $t \rightarrow 0$ and as $t \rightarrow d$. We can then expect the series in (3.12) to converge for $|t| \leq 1$.

To construct $G(t)$, we find the asymptotic behaviour of w near the singularities by performing local asymptotic analysis near D and as $x \rightarrow -\infty$.

The flow near D is a flow inside a corner. We will find the nature of the singularity at D by considering the general problem of a flow inside a corner of angle γ (see Figure 3.6).

We introduce cartesian coordinates with the origin at the apex G of the corner. We choose $\psi = 0$ on the streamline HGL and $\phi = 0$ at $x = y = 0$. Assuming without loss of generality that the flow is in the direction of the

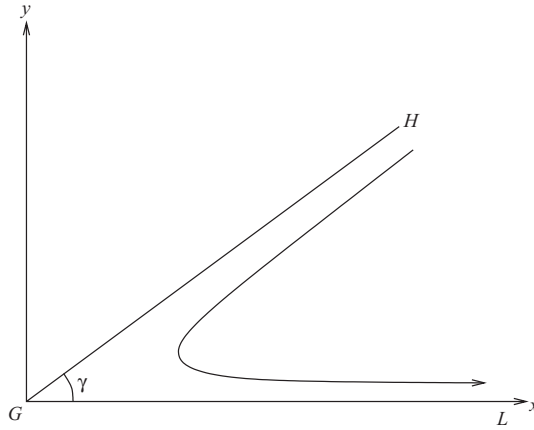


Fig. 3.6. Flow in a corner bounded by the walls GH and GL .

arrow, we have $\phi < 0$ along the wall HG , $\phi > 0$ along the wall GL and $\psi > 0$ in the flow domain. The flow configuration in the complex potential plane is shown in Figure 3.7.

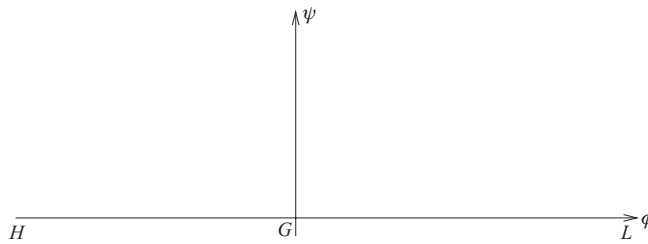


Fig. 3.7. The flow configuration of Figure 3.6 in the complex potential plane. The flow domain is the upper half-plane $\psi > 0$.

We seek a solution of the form

$$z = Ae^{i\alpha} f^\mu, \quad (3.13)$$

where $A > 0$, μ and α are real constants. On the wall GL (where $\phi > 0$), the kinematic boundary condition can be written as $\arg z = 0$. Therefore (3.13) implies that

$$\alpha = 0. \quad (3.14)$$

On the wall GH (where $\phi < 0$), the kinematic boundary condition can be

written as $\arg z = \gamma$. Writing $\phi = e^{i\pi}|\phi|$ and using (3.13), we find that

$$\alpha + \pi\mu = \gamma. \quad (3.15)$$

Relations (3.14) and (3.15) imply that

$$\mu = \frac{\gamma}{\pi}; \quad (3.16)$$

therefore (3.13) gives

$$z = Af^{\gamma/\pi}. \quad (3.17)$$

Since

$$w = \left(\frac{dz}{df}\right)^{-1} \quad (3.18)$$

we obtain the formula

$$w = \frac{\pi}{A\gamma} f^{1-\gamma/\pi} \quad (3.19)$$

or, eliminating f between (3.17) and (3.19),

$$w = \frac{\pi}{\gamma} A^{-\pi/\gamma} z^{\pi/\gamma-1}. \quad (3.20)$$

Flows inside corners will occur in many flow configurations described in this book and we will refer often to the above local analysis. We note that the formulae (3.17), (3.19) and (3.20) still hold if the boundary GL in Figure 3.6 is an arbitrary straight line through G (i.e. if the angle HGL is rotated). The only difference is that α is then different from zero.

The velocity at the point G is equal to zero when $\gamma < \pi$ and is unbounded when $\gamma > \pi$ see (3.20). We will refer to the flow of Figure 3.6 as a flow inside a corner when $\gamma < \pi$ and as a flow around a corner when $\gamma > \pi$.

For the flow of Figure 3.1, $\gamma = \pi - \gamma_2 + \gamma_1$ and (3.19) implies

$$w = O[(f - \phi_D - i)^{(\gamma_2 - \gamma_1)/\pi}] \quad \text{as } f \rightarrow \phi_D + i, \quad (3.21)$$

where ϕ_D is the value of ϕ at the point D . Here we have used the classical O notation to indicate an estimate of the behaviour of a function. We recall that writing

$$f(x) = O[g(x)] \quad \text{as } x \rightarrow x_0 \quad (3.22)$$

means that

$$\frac{f(x)}{g(x)} \rightarrow A \quad \text{as } x \rightarrow x_0, \quad (3.23)$$

where A is a constant. Similarly,

$$f(x) = o[g(x)] \quad \text{as } x \rightarrow x_0 \quad (3.24)$$

means that

$$\frac{f(x)}{g(x)} \rightarrow 0 \quad \text{as } x \rightarrow x_0. \quad (3.25)$$

Using (3.8) yields

$$f - \phi_D - i = O[t - d] \quad \text{as } f \rightarrow \phi_D + i. \quad (3.26)$$

Combining (3.21) and (3.26) gives

$$w = O[(t - d)^{(\gamma_2 - \gamma_1)/\pi}] \quad \text{as } t \rightarrow d. \quad (3.27)$$

This concludes our local analysis near the point D .

As $x \rightarrow -\infty$, the flow behaves like that due to a sink at $x = y = 0$. Therefore

$$f \approx -B \ln z \quad \text{as } x \rightarrow -\infty \quad (3.28)$$

where B is a positive constant. Differentiating (3.28) with respect to z gives

$$w = \frac{df}{dz} = -\frac{B}{z}. \quad (3.29)$$

Since the flux of the fluid coming from $-\infty$ is 1 and the angle between the walls CD and AB is γ_1 , we have

$$B = \frac{1}{\gamma_1}. \quad (3.30)$$

Eliminating z between (3.28) and (3.29) gives

$$w = O[e^{\gamma_1 f}] \quad \text{as } f \rightarrow -\infty, \quad (3.31)$$

and relation (3.8) then implies that

$$e^{\pi f} = O(t) \quad \text{as } f \rightarrow -\infty. \quad (3.32)$$

Therefore (3.31) and (3.32) give

$$w = O(t^{\gamma_1/\pi}) \quad \text{as } t \rightarrow 0. \quad (3.33)$$

Combining (3.27) and (3.33), we can choose

$$G(t) = (t - d)^{(\gamma_2 - \gamma_1)/\pi} t^{\gamma_1/\pi} \quad (3.34)$$

and write (3.12) as

$$w = (t - d)^{(\gamma_2 - \gamma_1)/\pi} t^{\gamma_1/\pi} \sum_{n=0}^{\infty} a_n t^n. \quad (3.35)$$

There are, of course, many other possible choices for $G(t)$. For example $G(t)$ in (3.34) can be multiplied by any function analytic in $|t| \leq 1$.

We now need to determine coefficients a_n in (3.35) such that the dynamic boundary condition (3.7) is satisfied. This can be done numerically by truncating the infinite series in (3.35) after N terms and finding the coefficients a_n , $n = 0, \dots, N - 1$ by collocation. This is the approach we will use when solving problems where the effects of gravity or surface tension are included in the dynamic boundary condition. However, it can be checked that

$$\sum_{n=0}^{\infty} a_n t^n = \left(\frac{1}{1 - td} \right)^{(\gamma_2 - \gamma_1)/\pi} \quad (3.36)$$

and therefore the present problem has the exact solution

$$w = \left(\frac{t - d}{1 - td} \right)^{(\gamma_2 - \gamma_1)/\pi} t^{\gamma_1/\pi}. \quad (3.37)$$

The existence of an exact solution for the flow of Figure 3.1 follows from the general theory of free streamline flows. This theory was developed by Kirchhoff [90] and Helmholtz [71]; see Birkhoff and Zarantonello [19] or Gurevich [69] for details.

The free surface profile is obtained by setting $\psi = 1$ in (3.8) and (3.37), calculating the partial derivatives x_ϕ and y_ϕ from the identity

$$x_\phi + iy_\phi = \frac{1}{w} \quad (3.38)$$

and integrating with respect to ϕ .

As a first example let us assume that $\gamma_1 = \gamma_2 = \pi/2$ (see Figure 3.2). Then (3.37) reduces to

$$w = t^{1/2} \quad (3.39)$$

and (3.9), (3.38) and (3.39) yield

$$x_\phi + iy_\phi = e^{-i\sigma/2}, \quad 0 < \sigma < \pi, \quad (3.40)$$

along the free surface EF . Differentiating (3.10) with respect to σ and applying the chain rule to (3.40) gives

$$x_\sigma + iy_\sigma = -\frac{1}{\pi} \cotan \frac{\sigma}{2} e^{-i\sigma/2}. \quad (3.41)$$

Integrating (3.41) with respect to σ and taking the real and imaginary parts gives

$$x = \frac{2}{\pi} \cotan \frac{\sigma}{2} + \frac{\sigma}{\pi} - 1 \quad (3.42)$$

$$y = \frac{2}{\pi} \sin \frac{\sigma}{2} + 1. \quad (3.43)$$

Relations (3.42) and (3.43) define the free surface profile in parametric form. It is shown in Figure 3.8.

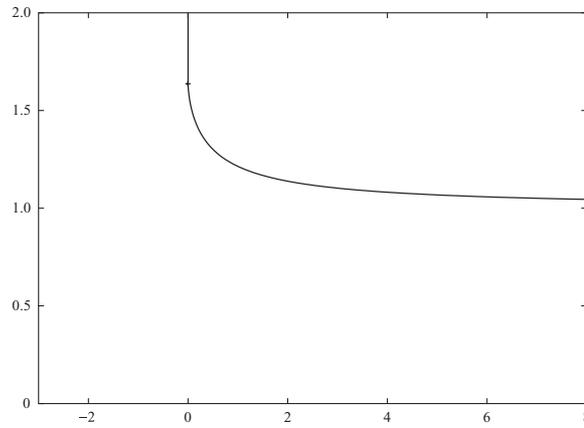


Fig. 3.8. Free surface profile for the flow configuration of Figure 3.2. The position of the separation point E is indicated by a small horizontal line. The vertical scale has been exaggerated to show clearly the free surface profile.

A classical parameter associated with this flow is the contraction ratio C_c , defined as the ratio y_F/y_E of the ordinates of the points F and E . Using (3.43) with $\sigma = \pi$ and $\sigma = 0$, we obtain

$$C_c = \frac{\pi}{\pi + 2} \approx 0.611. \quad (3.44)$$

As a second example, let us assume $\gamma_1 = 0$ and $\gamma_2 = \pi/2$ (see Figure 3.9). Then (3.37) becomes

$$w = \left(\frac{t-d}{1-td} \right)^{1/2}. \quad (3.45)$$

Proceeding as in the previous example, we obtain

$$x_\sigma + iy_\sigma = -\frac{1}{\pi} \cotan \frac{\sigma}{2} \left(\frac{1 - e^{i\sigma} d}{e^{i\sigma} - d} \right)^{1/2} \quad (3.46)$$

on the free surface EF .

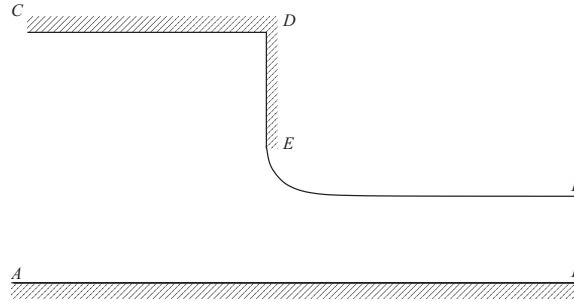


Fig. 3.9. A free surface flow emerging from a container bounded by the horizontal walls CD and AB and by the vertical wall DE .

Integrating (3.46) gives x and y on the free surface as functions of σ . There is a solution for each value of $-1 < d < 0$; the parameter d measures the length of the vertical wall DE in the complex t -plane. This is an inverse formulation in the sense that for each value of d the length of the wall DE in the physical plane is found at the end of the calculations, in the following way. We first calculate y_ϕ for $-1 < t < d$ by using (3.38) and (3.45). We then evaluate y_t for $-1 < t < d$ by using (3.8) and the chain rule. The length of the wall DE is then obtained by integrating with respect to t from -1 to d . A typical solution for $d = -0.5$ is shown in Figure 3.10.

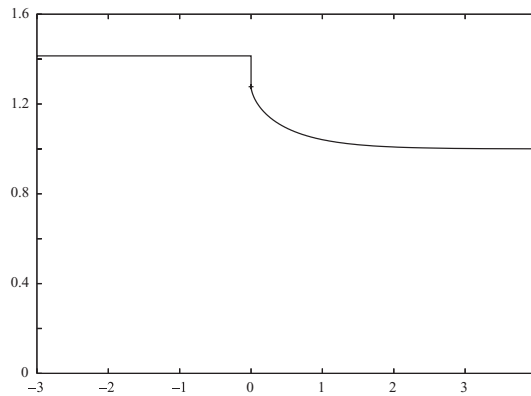


Fig. 3.10. Computed free surface profile for the flow configuration of Figure 3.9 with $d = -0.5$. The position of the separation point E is indicated by a small horizontal line. The vertical scale has been exaggerated to show clearly the free surface profile.

As $d \rightarrow 0$, the length of the vertical wall DE tends to infinity and the flow reduces to that of Figure 3.2. As $d \rightarrow -1$, the length of the vertical wall DE tends to zero and the flow reduces to a uniform stream.

As a third example, we assume $\gamma_2 < 0$ and $\gamma_1 = 0$ (see Figure 3.3). As mentioned at the beginning of this chapter, this configuration models the flow due to a surface-piercing obstacle moving at a constant velocity when viewed in a frame of reference moving with the obstacle. In particular it is a simple model for the flow near the stern or the bow of a ship. Again using (3.37), we obtain

$$w = \left(\frac{t-d}{1-t\bar{d}} \right)^{\gamma_2/\pi}. \quad (3.47)$$

As in the previous two examples we use (3.47) to calculate $x_\sigma + iy_\sigma$ on the free surface. After integration we obtain the shape of the free surface in parametric form. A typical free surface profile for $d = -0.2$ and $\gamma_2 = -\pi/3$ is shown in Figure 3.11.

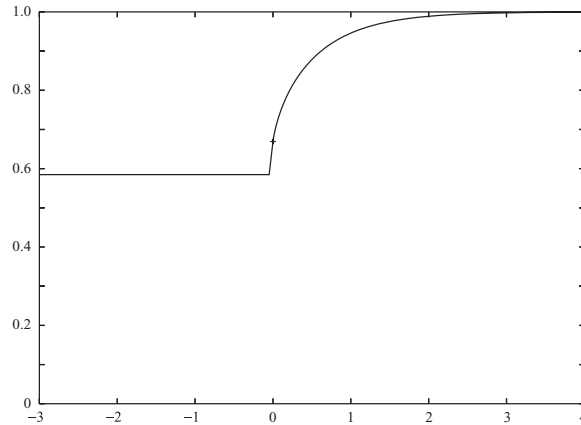


Fig. 3.11. Computed free surface profile for the flow configuration of Figure 3.3 with $d = -0.2$ and $\gamma_2 = -\pi/3$. The position of the separation point E is indicated by a small horizontal line. The vertical scale has been exaggerated to show clearly the free surface profile.

3.1.2 Free separation

In Figures 3.1 and 3.9, on the one hand, the free surface is forced to separate from the rigid wall DE at E because the wall DE terminates at E . We refer to this situation as forced separation. On the other hand, if the wall DE

is replaced by a smooth curve then in principle the point of separation E can be any point on the smooth curve (see Figure 3.12). We refer to this situation as free separation.

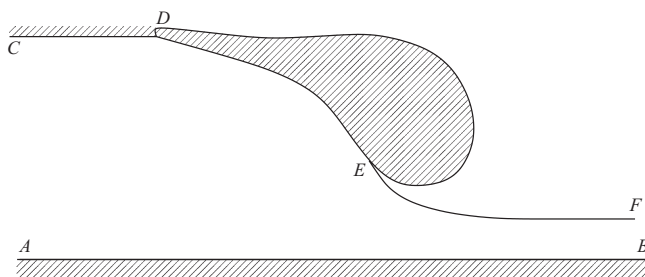


Fig. 3.12. The flow configuration of Figure 3.9 but with the vertical wall DE replaced by a smooth overhang.

We note that any solution corresponding to free separation represents also a solution with forced separation if a smooth curve forming an overhang is cut along a line through the separation point (see Figure 3.13). As we shall see in Section 3.2, the distinction between forced and free separation is important when studying the effects of surface tension.

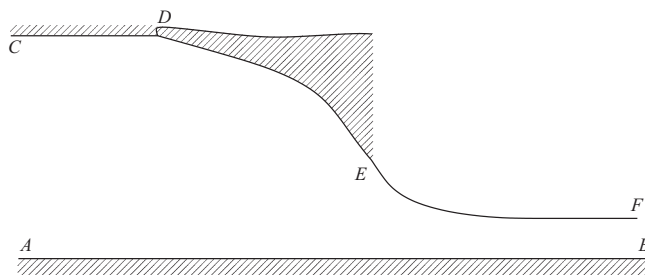


Fig. 3.13. The flow configuration of Figure 3.12 when the smooth surface is cut by a vertical line.

3.1.2.1 Open cavities

We now consider some solutions with free separation which will be useful in Section 3.2 when we consider the effects of surface tension. Figure 3.14 shows a particular case of Figure 3.12 for which the vertical rigid wall DE of Figure 3.9 has been replaced by a smooth ‘elliptical’ wall with equation

$$\left(\frac{\tilde{x}}{a}\right)^{1/2} + \left(\frac{\tilde{y}}{b}\right)^{1/2} = 1. \quad (3.48)$$

Here \tilde{x} and \tilde{y} refer to coordinates with the origin at the centre of the ellipse and \tilde{a} and \tilde{b} are the semi-axes of the ellipse.

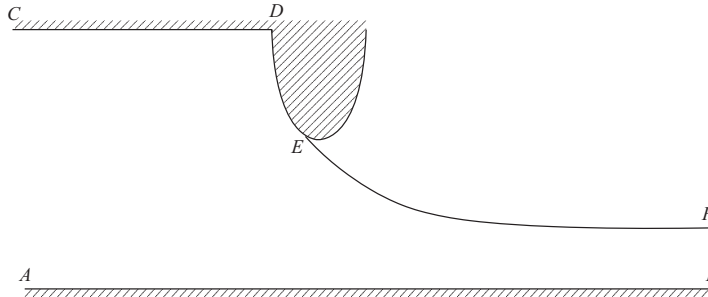


Fig. 3.14. The flow of Figure 3.9 when the vertical wall DE has been replaced by a smooth semi-elliptical wall.

If $\tilde{a} \ll \tilde{b}$, the semi-ellipse is thin and the configuration of Figure 3.14 can be viewed as that of Figure 3.9 but with the infinitely thin wall DE replaced by a smooth wall of finite thickness. In other words, Figure 3.14 takes into account the finite thickness of any real wall but approaches the configuration of Figure 3.9 as $\tilde{a}/\tilde{b} \rightarrow 0$. However, to study flows with free separation we shall assume that $\tilde{b} = \tilde{a}$ (i.e. that the semi-ellipse is a semicircle), so that flows corresponding to different positions of the separation point E can be clearly distinguished on the profiles.

The flow of Figure 3.14 can be reflected in the wall CD . This yields the flow of Figure 3.15. It models a flow past a circular cylinder with a cavity behind it (see for example Batchelor [8] for a discussion of cavitating flows).

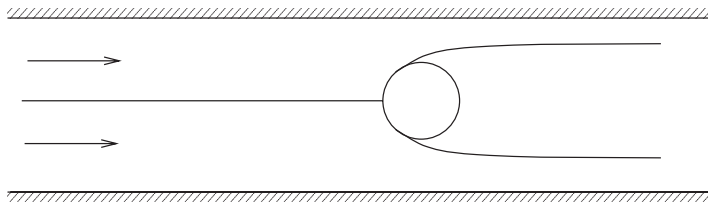


Fig. 3.15. Cavitating flow past a circular object in a domain bounded by two horizontal walls.

We shall study the flow of Figure 3.15 when the radius of the circle is very small compared with the distance between the horizontal walls, so that the circle can be assumed to be in a fluid unbounded in the vertical direction (see Figure 3.16). The angle between the free surface and the circle at the

separation points is denoted by β . For free streamline solutions $\beta = 0$. This follows from (3.20) with $\gamma = \beta$, which shows that a value $\beta \neq 0$ would generate a zero or an infinite velocity at the separation points. This would contradict (3.2). However, we shall see in Sections 3.2 and 3.4 that values $\beta \neq 0$ can occur when surface tension is taken into account.

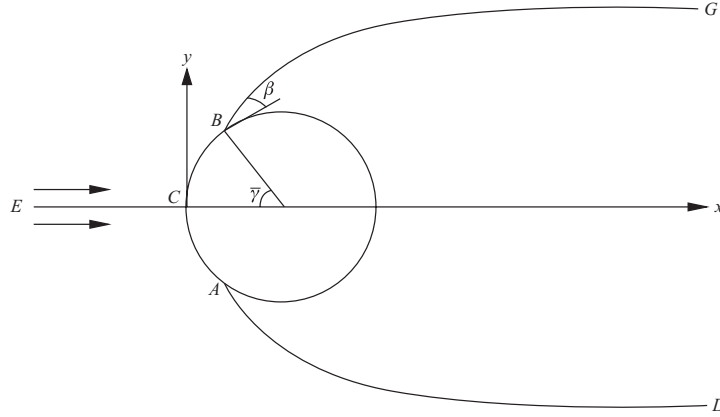


Fig. 3.16. The cavitating flow past a circle in an unbounded fluid domain. When the surface tension T is zero, the free surfaces leave the circle tangentially and $\beta = 0$. When $T \neq 0$, the angle β can be different from zero.

We define dimensionless variables by using the radius R of the circle as the reference length and the constant velocity U far upstream as the reference velocity. We introduce the potential function $b\phi$, the streamfunction $b\psi$ and the complex potential $f = b\phi + ib\psi$. Without loss of generality we may choose $\phi = 0$ at the point C and $\psi = 0$ on the streamlines $ECAD$ and $ECBG$. Here and in the remaining part of this section, the letters E, C, B, G, A and D refer to Figure 3.16. The constant b is defined so that $\phi = 1$ at the separation points A and B . The flow configuration in the complex potential plane is illustrated in Figure 3.17.

We introduce the complex velocity $u - iv$ and define the function $\tau - i\theta$ by the relation (3.3). Using (3.6), we have

$$K = -\frac{e^\tau}{b} \frac{\partial \theta}{\partial \phi}. \quad (3.49)$$

We shall seek $\tau - i\theta$ as an analytic function of $\phi + i\psi$ in the half-plane $\psi < 0$ (see Figure 3.17). The solution in $\psi > 0$ can then be obtained by symmetry. The boundary conditions on $\psi = 0$ are given by

$$\theta = 0 \quad \text{on} \quad \psi = 0, \quad -\infty < \phi < 0, \quad (3.50)$$

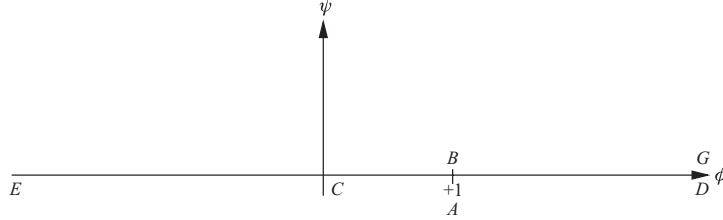


Fig. 3.17. The flow of Figure 3.16 in the complex potential plane.

$$\frac{e^\tau}{b} \frac{\partial \theta}{\partial \phi} = 1 \quad \text{on} \quad \psi = 0, \quad 0 < \phi < 1, \quad (3.51)$$

$$\tau = 0 \quad \text{on} \quad \psi = 0, \quad 1 < \phi < \infty. \quad (3.52)$$

The condition (3.50) follows from symmetry. Equation (3.51) follows from (3.49) and the fact that the curvature of the rigid boundary ACB is 1. Relation (3.52) is the dynamic boundary condition rewritten in terms of τ .

This completes the formulation of the problem. We seek $\tau - i\theta$ as an analytic function of $\phi + i\psi$ in $\psi < 0$ satisfying (3.50)–(3.52). We will solve the problem by following the series truncation method introduced in Section 3.1.1 (see (3.12)). First we map the flow domain into the unit circle in the complex t -plane by the transformation

$$f^{1/2} = \left(t - \frac{1}{t} \right) \frac{1}{2i}. \quad (3.53)$$

The flow configuration in the t -plane is shown in Figure 3.18. The rigid surface ACB is mapped onto the circle $|t| = 1$ and the free surfaces AD and BG are mapped onto the imaginary axis. The conditions (3.50)–(3.52) become

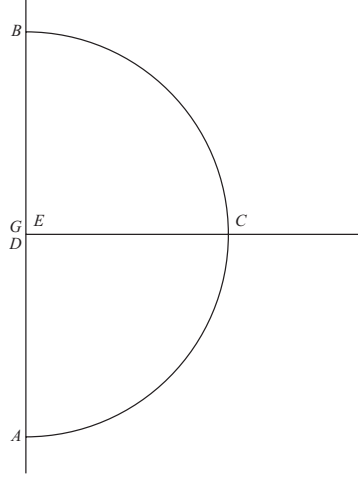
$$\theta = 0 \quad \text{on} \quad 0 < t < 1, \quad (3.54)$$

$$\frac{e^\tau}{b} \frac{\partial \theta}{\partial \phi} = 1 \quad \text{on} \quad t = e^{i\sigma}, \quad -\pi/2 < \sigma < 0, \quad (3.55)$$

$$\tau = 0 \quad \text{on} \quad t = ir, \quad -1 < r < 0. \quad (3.56)$$

Here we have described the unit circle $|t| = 1$ by $t = e^{i\sigma}$, where σ is a real parameter.

Following Brodetsky [23] and Vanden-Broeck [160] we represent $\tau - i\theta$ by

Fig. 3.18. Sketch of the flow of Figure 3.16 in the complex t -plane.

an expansion, as follows:

$$\tau - i\theta = -\ln \frac{1+t}{1-t} - \sum_{n=0}^{\infty} B_n t^n. \quad (3.57)$$

The derivation of (3.57) follows that leading to (3.12). There is a singularity at the point C where locally we have a flow inside a right angle corner (see Figure 3.16). Therefore, (3.19) yields

$$u - iv \sim f^{1/2} \quad \text{as } f \rightarrow 0. \quad (3.58)$$

Using (3.3) and (3.53) yields $\tau - i\theta \sim \ln(1-t)$ as $t \rightarrow 1$. Thus

$$\tau - i\theta + \ln \frac{1+t}{1-t} \quad (3.59)$$

is not singular and can be represented in the unit circle of the t -plane by a Taylor expansion. This leads to (3.57). One might argue that other singularities occur at the separation points A and B . However, these singularities are automatically taken into account by (3.53). We note that (3.57) implies

$$u - iv = G(t) \exp \left(- \sum_{n=0}^{\infty} B_n t^n \right), \quad (3.60)$$

where

$$G(t) = \frac{1-t}{1+t}. \quad (3.61)$$

Therefore (3.60) is similar to (3.12). The only difference is that the series has been rewritten as the exponential of a series.

It can easily be checked that (3.54) and (3.56) are satisfied by assuming that the coefficient B_n is real and that $B_n = 0$ when n is even. Therefore we can rewrite (3.57) as

$$\tau - i\theta = -\ln \frac{1+t}{1-t} + \sum_{n=1}^{\infty} A_n t^{2n-1}. \quad (3.62)$$

We now determine coefficients A_n such that (3.55) is satisfied. This is done numerically by series truncation and collocation. Thus we truncate the infinite series in (3.62) after N terms, i.e. we write

$$\tau - i\theta \approx -\ln \frac{1+t}{1-t} + \sum_{n=1}^N A_n t^{2n-1}. \quad (3.63)$$

Next, we satisfy (3.55) at the mesh points $\sigma = \sigma_I$, where

$$\sigma_I = -\frac{\pi}{2N}I, \quad I = 1, 2, \dots, N. \quad (3.64)$$

This is achieved by using (3.62) to evaluate the values of τ , θ and $\partial\theta/\partial\phi$ at the mesh points (3.64) and substituting these values into (3.55). This leads to a system of N equations for the $N+1$ unknowns A_n , $n = 1, 2, \dots, N$, and b . The last equation is obtained by fixing the position of the separation point A . This is done by imposing

$$\theta(\sigma_N) = \bar{\gamma} - \frac{\pi}{2}, \quad (3.65)$$

where the angle $\bar{\gamma}$ is defined in Figure 3.16.

The system of $N+1$ nonlinear algebraic equations with $N+1$ unknowns needs to be solved numerically by iteration. In most problems considered in this book, this is done by Newton's method. This method can be described as follows. Assume that we want to solve a system of M nonlinear algebraic equations

$$f_i(x_1, x_2, \dots, x_M) = 0, \quad i = 1, 2, \dots, M, \quad (3.66)$$

with M unknowns x_1, x_2, \dots, x_M . Let $(x_1^{(n)}, x_2^{(n)}, \dots, x_M^{(n)})$ be the approximation of the solution at iteration n . Then we linearise the left-hand side of (3.66) around this iteration as

$$f_i(x_1^{(n)}, x_2^{(n)}, \dots, x_M^{(n)}) + \sum_{j=1}^M (x_j - x_j^{(n)}) \left(\frac{\partial f_i}{\partial x_j} \right)^{(n)}. \quad (3.67)$$

The next approximation, $(x_1^{(n+1)}, x_2^{(n+1)}, \dots, x_M^{(n+1)})$, is obtained by equating (3.67) to zero and solving the resulting linear system for x_1, x_2, \dots, x_M . Each iteration is expensive since it requires solving a linear system of equations. However, the iterations usually converge quadratically so that only a few iterations are needed to obtain an accurate solution. The method also requires an initial guess $(x_1^{(0)}, x_2^{(0)}, \dots, x_M^{(0)})$ to start the iterative process. When facing a problem with several solutions, the solution obtained after convergence will depend on the initial guess chosen. The matrix with elements

$$\frac{\partial f_i}{\partial x_j} \quad (3.68)$$

is called the Jacobian matrix; an attractive feature of Newton's method is that bifurcations from branches of solutions can be found by monitoring the sign of its determinant. This is a consequence of the fact that the determinant vanishes at a bifurcation point (Keller [84]).

The free surface profiles are then obtained by integrating numerically the identity

$$\frac{1}{b} \left(\frac{\partial x}{\partial \phi} + i \frac{\partial y}{\partial \phi} \right) = e^{-\tau + i\theta}. \quad (3.69)$$

The numerical results can be described in terms of the angle $\bar{\gamma}$. Solutions can be obtained for all values $0 < \bar{\gamma} < \pi$. However, only the solutions for $\gamma^* < \bar{\gamma} < \gamma^{**}$, where $\gamma^* \approx 55^\circ$ and $\gamma^{**} \approx 124^\circ$, have a physical meaning for cavitating flow past a circle.

For $\bar{\gamma} < \gamma^*$ the solutions are not acceptable because then the free surfaces would enter the body (see the solution for $\bar{\gamma} = 25^\circ$ in Figure 3.19). They are nevertheless useful in describing the cavitating flow past the body obtained by cutting the circle along the straight line AB in Figure 3.16 and retaining only the portion on the left of AB . This cutting of the circle is similar to the cutting seen in Figure 3.13.

For $\bar{\gamma} > \gamma^{**}$ the solutions are not acceptable because the free surfaces cross each other (see the solution for $\bar{\gamma} = 150^\circ$ in Figure 3.19). The last acceptable solution, at $\bar{\gamma} = \gamma^{**}$, has free surfaces that approach the x -axis asymptotically as $x \rightarrow \infty$ (see Figure 3.20).

Physically acceptable solutions for $\bar{\gamma} > \gamma^{**}$ can be obtained by considering cusped cavities. Cusped cavities were introduced numerically by Southwell and Vaisey [142] and analytically by Lighthill [98] and [99]. They will be calculated numerically by a boundary integral equation method in the next section.

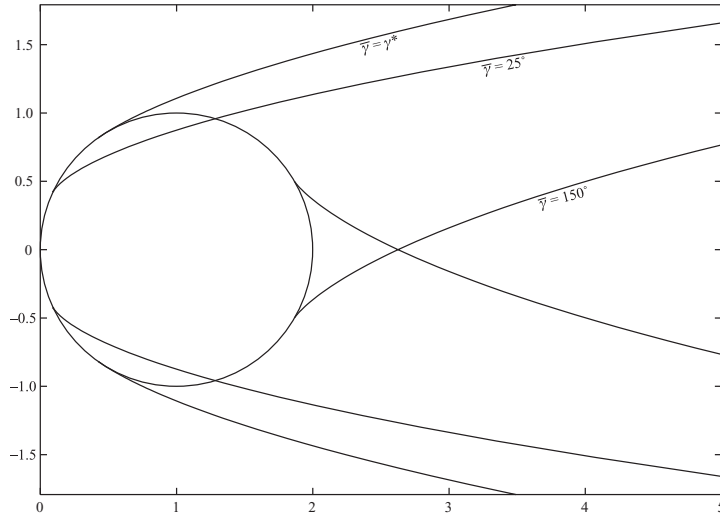


Fig. 3.19. Computed free surface profiles for $\bar{\gamma} = 25^\circ$, $\bar{\gamma} = \gamma^*$ and $\bar{\gamma} = 150^\circ$.

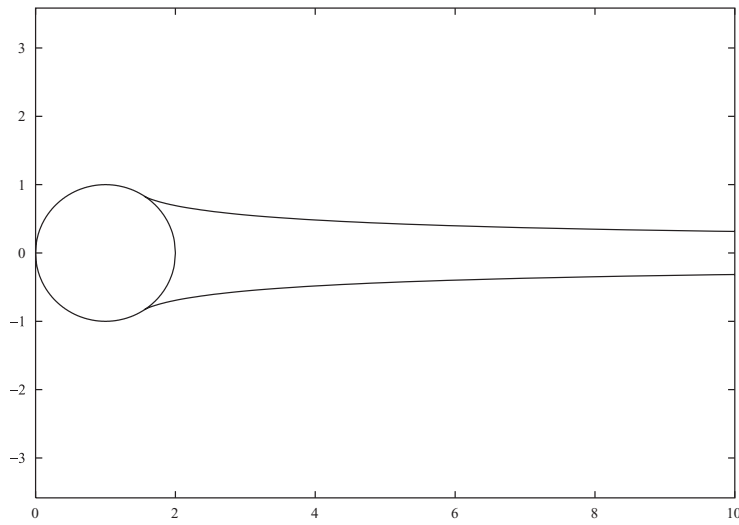


Fig. 3.20. The cavitating flow corresponding to $\bar{\gamma} = \gamma^{**} \approx 124^\circ$.

3.1.2.2 Cusped cavities

Unwanted intersections of free surfaces, such as those described above for $\bar{\gamma} > \gamma^{**}$, occur in many applications. A classical example is the exact solution of Crapper [37] for nonlinear capillary waves, travelling at a constant

velocity at the surface of a fluid of infinite depth (see Section 6.5.1 and Figures 6.8–6.11). Crapper’s solutions form a one-parameter family of solutions. The parameter can be chosen as the steepness s of the waves (i.e. the difference in height of the crests and the troughs divided by the wavelength). For small values of s , the waves are close to linear sine waves (see Figure 6.8). As s increases the waves develop rounded crests and sharp troughs (see Figure 6.9). When s reaches the critical value $s^* \approx 0.73$, the free surface develops a point of contact with itself and a small trapped bubble forms at the trough of the wave (see Figure 6.10). For $s > s^*$, the free surface is self-intersecting and the solutions lose their physical meaning (see Figure 6.11). Vanden-Broeck and Keller [185] showed that physically acceptable solutions for $s > s^*$ can be obtained by preventing the free surface from self-intersecting. The resulting free surface profiles for $s > s^*$ have trapped bubbles at the troughs, as in Crapper’s solution for $s = s^*$. Since preventing self-intersection imposes an extra constraint on the solutions, an extra unknown is needed. This is provided by the pressure in the trapped bubble, which is found as part of the solution.

The calculations of Vanden-Broeck and Keller [185] will be described in Section 6.5.1. Here we use a similar approach to find physically acceptable cavitating flows for $\bar{\gamma} > \gamma^{**}$, by preventing the crossing of the streamlines and seeking a family of cusped cavities (see Figure 3.21).

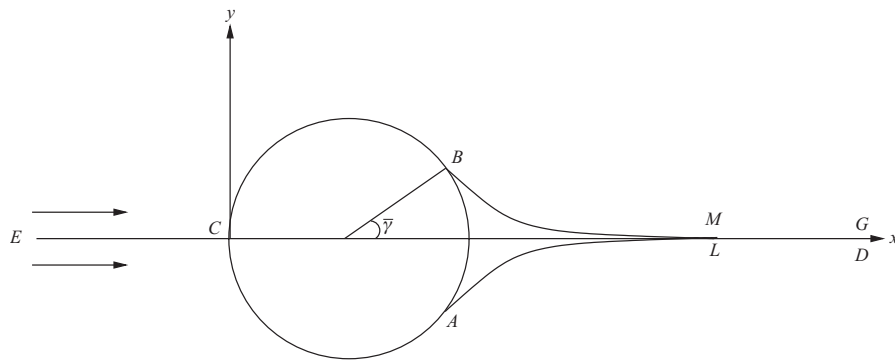


Fig. 3.21. Flow past a circle giving rise to a cusped cavity.

As we shall see there is a cusped cavity for each value of $\bar{\gamma} > \gamma^{**}$. These solutions approach the solution in Figure 3.20 as $\bar{\gamma} \rightarrow \gamma^{**}$. In other words the x -coordinate of the cusp in Figure 3.21 tends to ∞ as $\bar{\gamma} \rightarrow \gamma^{**}$ and the corresponding solution approaches that of Figure 3.20. As $\bar{\gamma} \rightarrow 180^\circ$, the x -coordinate of the cusp tends to 2 and the cavity collapses to a point.

Following the work of Vanden-Broeck and Keller [185], as mentioned above we need to identify a new unknown to prevent the intersection of the free streamlines. A natural choice is the pressure p_c in the cavity. This is motivated by the fact that cusped cavities are closed (they do not extend to infinity as do the open cavities of Figure 3.19) and so we do not have to require that $p_c = p_b$. Therefore our dynamic boundary condition on the free surfaces AL and BM of Figure 3.21 is

$$\tau = \frac{1}{2} \ln(1 + \mathcal{C}), \quad (3.70)$$

where the cavitation number \mathcal{C} is found as part of the solution. We define the potential function $b\phi$ and the streamfunction $b\psi$ and choose b so that $\phi = 1$ at the separation points B and A . The flow configuration in the complex (ϕ, ψ) -plane is illustrated in Figure 3.22.

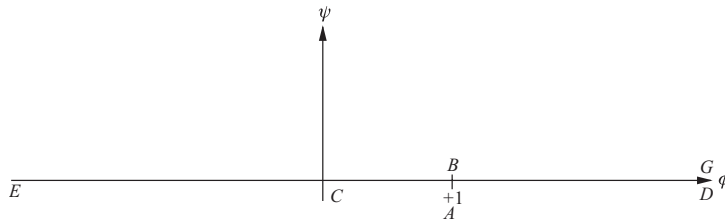


Fig. 3.22. The flow of Figure 3.21 in the complex-potential plane.

We solve the problem by a boundary integral equation method. This technique will be used extensively in the remaining part of the book. The basic idea is to reformulate the problem as a system of integro-differential equations that involves only unknowns on the boundary of the flow domain. This system is then discretised and the resultant algebraic equations are solved by iteration (usually Newton iteration). The obvious advantage is that mesh points are only needed on the boundary rather than in the whole flow domain. In other words the two-dimensional flow problem of Figure 3.21 is reduced to a one-dimensional problem on the boundary $ECALD$. As we shall see in Chapter 10, boundary integral equation methods can also be used for solving fully three-dimensional problems. There the three-dimensional problem is reduced to a two-dimensional problem on the boundary. A convenient way of deriving the system of integro-differential equations for two-dimensional flows is to use the Cauchy's integral equation formula (see (2.38)–(2.41)). An alternative way which does not rely on complex variables is to use Green's theorem and Green's functions. For

three-dimensional problems, complex variables are not available and Green's theorem and Green's functions are the only way to derive the system of integro-differential equations.

We can derive such a system for the problem of Figure 3.21 by applying the Cauchy integral equation formula in the (ϕ, ψ) -plane to the function $\tau(\phi, \psi) - i\theta(\phi, \psi)$ with a contour consisting of the axis $\psi = 0$ and a semicircle in $\psi < 0$ centred on $\phi = \psi = 0$ and of arbitrary large radius. Since $\tau(\phi, \psi) - i\theta(\phi, \psi) \rightarrow 0$ as $\psi \rightarrow -\infty$, there is no contribution from the semicircle and we obtain

$$\tau(\phi, \psi) - i\theta(\phi, \psi) = -\frac{1}{2i\pi} \int_{-\infty}^{\infty} \frac{\tau(\varphi, 0) - i\theta(\varphi, 0)}{\varphi - \phi - i\psi} d\varphi \quad \text{when } \psi < 0. \quad (3.71)$$

(see (2.40)). On the free surface, (2.41) gives

$$\tau(\phi, 0) - i\theta(\phi, 0) = -\frac{1}{i\pi} \int_{-\infty}^{\infty} \frac{\tau(\varphi, 0) - i\theta(\varphi, 0)}{\varphi - \phi} d\varphi. \quad (3.72)$$

The integral in (3.72) is a Cauchy principal value. Taking the real and imaginary parts of (3.72) gives

$$\tau(\phi, 0) = \frac{1}{\pi} \int_{-\infty}^{\infty} \frac{\theta(\varphi, 0)}{\varphi - \phi} d\varphi, \quad (3.73)$$

$$\theta(\phi, 0) = -\frac{1}{\pi} \int_{-\infty}^{\infty} \frac{\tau(\varphi, 0)}{\varphi - \phi} d\varphi. \quad (3.74)$$

Relations (3.73) and (3.74) are known as Hilbert transforms. It can be shown that one implies the other. Therefore we are free to choose either (3.73) or (3.74). It turns out that (3.73) is the better choice because it leads to a relation between τ and θ on the portion CAL of the streamline $\psi = 0$. This follows from the fact that $\theta = 0$ on EC and on LD . Therefore (3.73) simplifies to

$$\tau(\phi, 0) = \frac{1}{\pi} \int_0^l \frac{\theta(\varphi, 0)}{\varphi - \phi} d\varphi. \quad (3.75)$$

Here l is the value of ϕ at the cusp L . If we restrict the values of ϕ in (3.75) to $0 < \phi < l$, then (3.75) is a relation between τ and θ on CAL .

The kinematic boundary condition on CA and the dynamic boundary condition (3.70) imply that

$$\frac{e^\tau}{b} \frac{\partial \theta}{\partial \phi} = 1, \quad 0 < \phi < 1, \quad (3.76)$$

$$\tau = \frac{1}{2} \ln(1 + \mathcal{C}), \quad 1 < \phi < l. \quad (3.77)$$

Finally, we impose $y = 0$ at the cusp by writing

$$\int_0^l e^{-\tau(\varphi,0)} \sin \theta(\varphi,0) d\varphi = 0. \quad (3.78)$$

This completes the reformulation of the problem as a system of nonlinear integro-differential equations. We seek $\tau(\phi, 0)$ and $\theta(\phi, 0)$ such that (3.75)–(3.78) are satisfied. Once $\tau(\phi, 0)$ and $\theta(\phi, 0)$ are known for $0 < \phi < l$, then the shape of the cusped cavity and the velocity field in the flow domain can be calculated by integration in the following way. First the shape of the cavity is obtained in the parametric form $x(\phi, 0)$, $y(\phi, 0)$ by integrating the identity

$$x_\phi + iy_\phi = \frac{1}{u - iv} = e^{-\tau(\phi,0) + i\theta(\phi,0)}. \quad (3.79)$$

Next, $\tau(\phi, 0)$ for $\phi < 0$ and $\phi > l$ can be calculated from (3.75). The values of $\tau(\phi, 0)$ and $\theta(\phi, 0)$ are then known for all $-\infty < \phi < \infty$. Substituting these values in (3.71), we can evaluate by integration $\tau(\phi, \psi)$ and $\theta(\phi, \psi)$ everywhere in the flow domain. The velocity field is then given by (3.3).

We will solve the problem numerically. First we define the mesh points

$$\phi_I = \frac{I-1}{N-1}, \quad I = 1, \dots, M, \quad (3.80)$$

and the corresponding unknowns

$$\theta_I = \theta(\phi_I, 0), \quad I = 1, \dots, M, \quad (3.81)$$

where M and N are positive integers and $l = (M-1)/(N-1)$. Since $l > 1$, we require $M > N$. We also use the midpoints

$$\phi_I^m = \frac{\phi_I + \phi_{I+1}}{2}, \quad I = 1, \dots, M-1. \quad (3.82)$$

We calculate $\tau(\phi_I^m)$ in terms of the unknowns (3.81) by applying the trapezoidal rule to the integral in (3.75) and summing over the points (3.80). We justify this discretisation by showing that the symmetry of the quadrature and of the distribution of mesh points enable us to calculate the Cauchy principal value as if it were an ordinary integral. First we rewrite the integral on the right-hand side of (3.75) (evaluated at ϕ_I^m) as

$$\int_0^{\phi_I} \frac{\theta(\varphi, 0)}{\varphi - \phi_I^m} d\varphi + \int_{\phi_I}^{\phi_{I+1}} \frac{\theta(\varphi, 0)}{\varphi - \phi_I^m} d\varphi + \int_{\phi_{I+1}}^l \frac{\theta(\varphi, 0)}{\varphi - \phi_I^m} d\varphi. \quad (3.83)$$

The first and third integrals in (3.83) are ordinary integrals and can therefore

be evaluated by the trapezoidal rule. The second integral in (3.83) is a Cauchy principal value, which we rewrite as

$$\int_{\phi_I}^{\phi_{I+1}} \frac{\theta(\varphi, 0) - \theta(\phi_I^m, 0)}{\varphi - \phi_I^m} d\varphi + \theta(\phi_I^m, 0) \int_{\phi_I}^{\phi_{I+1}} \frac{d\varphi}{\varphi - \phi_I^m}. \quad (3.84)$$

The second integral in (3.84) is also a Cauchy principal value. Simple integration shows that its value is zero. The first integral in (3.84) is an ordinary integral and can be evaluated by the trapezoidal rule as

$$\frac{\theta_I - \theta(\phi_I^m, 0) h}{\phi_I - \phi_I^m} \frac{h}{2} + \frac{\theta_{I+1} - \theta(\phi_I^m, 0) h}{\phi_{I+1} - \phi_I^m} \frac{h}{2} = \frac{\theta_{I+1}}{\phi_{I+1} - \phi_I^m} \frac{h}{2} + \frac{\theta_I}{\phi_I - \phi_I^m} \frac{h}{2}. \quad (3.85)$$

The right-hand side of (3.85) is just the integral

$$\int_{\phi_I}^{\phi_{I+1}} \frac{\theta(\varphi, 0)}{\varphi - \phi_I^m} d\varphi$$

evaluated by the trapezoidal rule. Therefore the Cauchy principal value on the right-hand side of (3.75) can be evaluated by the trapezoidal rule as if it were an ordinary integral. This approach to evaluating Cauchy principal values will be used often in this book. We note that the derivation (3.83)–(3.85) can easily be extended to other integration formulae such as Simpson's rule or for mesh points ϕ_I^M that are not midpoints. The only differences are that the second integral in (3.84) might not be zero and that the left-hand side of (3.85) should be used instead of the right-hand side.

We now return to our problem and satisfy (3.76) at the mesh points ϕ_I^m , $I = 2, \dots, N-1$, and (3.77) at the mesh points ϕ_I^m , $I = N, \dots, M-2$. The last three equations are given by (3.78) and by the geometric conditions

$$\theta_1 = -\frac{\pi}{2}, \quad \theta_M = 0. \quad (3.86)$$

This system of algebraic equations is solved by Newton's method. Typical free surface profiles are shown in Figure 3.23.

It can be seen that as $\bar{\gamma} \rightarrow \gamma^{**}$, $\mathcal{C} \rightarrow 0$ and as $\bar{\gamma} \rightarrow 180^\circ$, $\mathcal{C} \rightarrow -\infty$.

We note that the numerical procedure presented here is not restricted to a circular obstacle and can be generalised to ones of arbitrary shapes in the following way. First we denote by $F(x, y) = 0$ the equation of the rigid boundary CA (see Figure 3.21) and calculate x and y on CA by the formulae

$$x(\phi, 0) = \int_0^\phi e^{-\tau(\varphi, 0)} \cos \theta(\varphi, 0) d\varphi \quad (3.87)$$

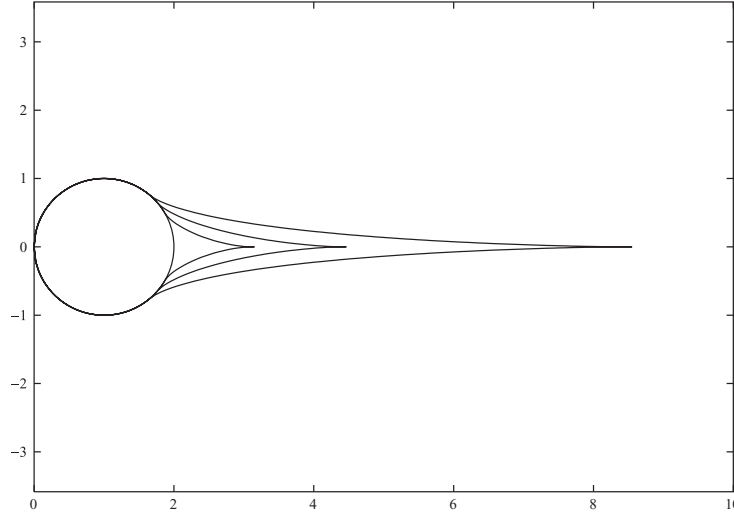


Fig. 3.23. Three computed cusped cavities. The cavitation numbers \mathcal{C} from the smallest cavity to the largest are -0.55 , -0.29 and -0.1 respectively.

and

$$y(\phi, 0) = \int_0^\phi e^{-\tau(\varphi, 0)} \sin \theta(\varphi, 0) d\varphi. \quad (3.88)$$

We then apply the numerical procedure described above, the equations obtained by satisfying (3.76) at the mesh points ϕ_I^m , $I = 2, \dots, N - 1$, being replaced by the new equations

$$F[x(\phi_I^m, 0), y(\phi_I^m, 0)] = 0, \quad I = 2, \dots, N - 1, \quad (3.89)$$

where $x(\phi, 0)$ and $y(\phi, 0)$ are defined by (3.87) and (3.88).

The solutions derived in this section are examples of cavitating flows with $\mathcal{C} < 0$. Such cavities were considered analytically by Lighthill [98], [99]. Batchelor [8] notes that such cavities have not been observed, perhaps because the boundary layer at the rigid surface would separate before reaching the low-velocity region where the free streamlines begin.

Before concluding this section, let us mention that there are many cavity models with $\mathcal{C} > 0$ (the Riabouchinsky model, the re-entrant jet model, the Roskho model etc). The reader interested in these models is referred to the books of Birkhoff and Zarantonello [19] and Gurevich [69].

3.2 The effects of surface tension

In this section we will investigate the effects of the surface tension T on the free streamline solutions of Section 3.1. We show that the limit $T \rightarrow 0$ is singular. When $T \neq 0$, discontinuities in slope can appear at the separation points. In particular, values of $\beta \neq 0$ can occur in Figure 3.16. We shall also show that the limit $T \rightarrow 0$ can be used to select solutions.

3.2.1 Forced separation

We start our study by investigating the local behaviour of the flow of Figure 3.1 near the separation point E , in the absence of surface tension. For simplicity we assume $\gamma_1 = \gamma_2 = \pi/2$, i.e. we consider the flow shown in Figure 3.2. The point E corresponds to $t = -1$, $\psi = 1$ and $\phi = 0$. Using (3.8) we find

$$\phi \approx -\frac{1}{4\pi}(t+1)^2 \quad \text{as } t \rightarrow -1. \quad (3.90)$$

Relation (3.39) gives

$$w \approx i - \frac{i}{2}(t+1) \quad \text{as } t \rightarrow -1. \quad (3.91)$$

Furthermore (3.3) gives

$$w \approx i + \theta + \frac{\pi}{2} \quad \text{as } t \rightarrow -1. \quad (3.92)$$

Combining (3.90)–(3.92), we obtain

$$\theta \approx -\frac{\pi}{2} + (\pi\phi)^{1/2}. \quad (3.93)$$

Since $e^\tau = 1$ at E , (3.6) implies that

$$K \approx -S\phi^{-1/2} \quad \text{as } \phi \rightarrow 0, \quad (3.94)$$

where

$$S = \frac{1}{2}\pi^{1/2}. \quad (3.95)$$

Therefore the flow leaves the wall DE tangentially (see (3.93)) but the curvature of the free surface at E is unbounded (see (3.94)). It can be shown that (3.94) holds for $\gamma_1 \neq \pi/2$ and $\gamma_2 \neq \pi/2$. Of course, the value of S depends on γ_1 and γ_2 .

These free streamline results show that an infinite curvature can occur at the separation points. This singularity does not invalidate the free streamline theory because the curvature does not appear explicitly in the equations

and does not have a direct physical meaning. However, when surface tension is taken into account, the condition $p = p_a$ on the free surface is replaced by

$$p = p_a + TK, \quad (3.96)$$

where T is the surface tension and K is the curvature of the free surface (see (2.19)). It follows from (3.1) and (3.96) that the dynamic boundary condition on the free surface becomes

$$\frac{1}{2}(u^2 + v^2) + \frac{T}{\rho}K = \text{constant}. \quad (3.97)$$

Equation (3.97) shows that an infinite curvature at the separation point E implies an infinite velocity at E . This implies that solutions with $T \neq 0$ are qualitatively different from the solutions with $T = 0$ of Section 3.1.1. It also suggests that the limit $T \rightarrow 0$ is a singular limit. These two properties are confirmed by the calculations below.

Ackerberg [2], Cumberbatch and Norbury [39], Vanden-Broeck ([159], [160], [163], [164], [176]) and others studied the flow configuration of Figure 3.2 (and related free surface flows) in the limit as $T \rightarrow 0$. The results of Vanden-Broeck showed that the inclusion of surface tension in the free streamline flows of Section 3.1.1 does not remove the infinite curvature at the separation points. On the contrary, it makes the flow more singular by introducing a discontinuity in slope at the separation points. In other words there is an angle $\beta \neq 0$ between the tangent to the free surface at the separation point and the wall (see Figure 3.24).

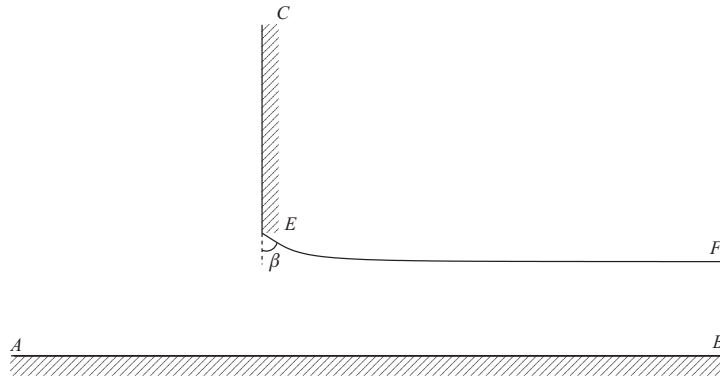


Fig. 3.24. The flow under a gate with surface tension included in the dynamic boundary condition. The free surface does not leave the gate tangentially: there is an angle $\beta \neq 0$ between the free surface and the gate at the separation point E .

This angle β is a function of the surface tension. We now demonstrate

these findings by presenting asymptotic results, for T small. We will present later fully nonlinear computations for arbitrary values of T .

We assume that the flow in Figure 3.24 is characterised by a uniform stream with constant velocity U as $x \rightarrow \infty$. As in Section 3.1.1, we define dimensionless variables by taking U as the unit velocity and $H = Q/U$ (for Q see Figure 3.4) as the unit length. The dynamic boundary condition (3.97) in dimensionless form is then

$$\frac{1}{2}(u^2 + v^2) + \frac{1}{\alpha}K = \text{constant}, \quad (3.98)$$

where

$$\alpha = \frac{\rho U^2 H}{T}. \quad (3.99)$$

Since $u^2 + v^2 \rightarrow 1$ and $K \rightarrow 0$ as $\phi \rightarrow \infty$, the constant on the right-hand side of (3.98) is equal to $1/2$. Using (3.3) and (3.6), we rewrite (3.98) as

$$\frac{1}{2}e^{2\tau} - \frac{1}{\alpha}e^\tau \frac{\partial \theta}{\partial \phi} = \frac{1}{2}. \quad (3.100)$$

If we assume $\phi = 0$ at the separation point then the free streamline solution (i.e. the solution for $\alpha = \infty$) for the configuration of Figure 3.1 can be described near the separation point by

$$\theta \approx \theta_0 - C\phi^{1/2} \quad \text{as } \phi \rightarrow 0, \quad (3.101)$$

where C is a constant. Here θ_0 is the value of θ at the separation point when $\alpha = \infty$. For example, for the flow of Figure 3.24, (3.93) shows that

$$C = -\pi^{1/2} \quad \text{and} \quad \theta_0 = -\pi/2. \quad (3.102)$$

Relation (3.101) implies that the curvature of the free surface near E behaves like

$$K = -e^\tau \frac{\partial \theta}{\partial \phi} \approx \frac{1}{2}C\phi^{-1/2} \quad \text{as } \phi \rightarrow 0. \quad (3.103)$$

Therefore the curvature of the free surface is unbounded at the separation point E unless $C = 0$.

Following Ackerberg [2] we introduce the following scaling of the variables:

$$f^* = \alpha f, \quad (3.104)$$

$$\tau^* - i\theta^* = \alpha^{1/2}(\tau - i\theta + i\theta_0). \quad (3.105)$$

The function τ^* satisfies Laplace's equation in $\psi^* < 0$. Thus

$$\frac{\partial^2 \tau^*}{\partial \phi^{*2}} + \frac{\partial^2 \tau^*}{\partial \psi^{*2}} = 0. \quad (3.106)$$

The kinematic and dynamic boundary conditions linearise in the limit $\alpha \rightarrow \infty$, so that the boundary conditions on $\psi^* = 0$ are

$$\frac{\partial \tau^*}{\partial \psi^*} = 0 \quad \text{on} \quad \psi^* = 0, \quad \phi^* < 0, \quad (3.107)$$

$$\frac{\partial \psi^*}{\partial \psi^*} = 0 \quad \text{on} \quad \psi^* = 0, \quad \phi^* > 0. \quad (3.108)$$

Relation (3.101) gives the outer behaviour

$$\tau^* \approx \Im C (f^*)^{1/2} \quad \text{as} \quad |f^*| \rightarrow \infty, \quad (3.109)$$

where \Im indicates the imaginary part of a function. Cumberbatch and Norbury [39] showed that the solution of (3.106)–(3.108) not containing waves and having the weakest singularity at the separation point $\phi^* = 0$ is given on the free surface by

$$\theta^*(\phi^*) = \frac{1}{2} C \pi^{1/2} + \frac{C}{2\pi^{1/2}} \phi^* \ln \phi^* \quad \text{as} \quad \phi^* \rightarrow 0, \quad (3.110)$$

$$\tau^*(\phi^*) = \frac{1}{2\pi^{1/2}} C \ln \phi^* \quad \text{as} \quad \phi^* \rightarrow 0. \quad (3.111)$$

The solution (3.110), (3.111) is not valid near $\phi^* = 0$ because τ^* is unbounded at $\phi^* = 0$ (an unbounded value of τ^* invalidates the linearisation).

The asymptotic scheme can now be described as follows. For ϕ large we have an outer solution whose first term is the free streamline solution (i.e. the solution without surface tension). This solution merges with the solution (3.110), (3.111) obtained for $\phi^* \approx 1$, i.e. for $\phi \approx \alpha^{-1}$. Since the solution (3.110), (3.111) becomes invalid as $\phi^* \rightarrow 0$, we follow Vanden-Broeck [159] and seek a local solution that corresponds to a flow past a corner of angle γ_0 . Thus on the one hand, using (3.19) and (3.3), we can write

$$e^\tau = \frac{\pi}{A\gamma_0} \phi^{\pi/\gamma_0 - 1}, \quad (3.112)$$

which implies that, near $\phi = 0$,

$$\tau \approx \left(1 - \frac{\gamma_0}{\pi}\right) \ln \phi. \quad (3.113)$$

On the other hand (3.105) and (3.111) give

$$\tau = \frac{\tau^*}{\alpha^{1/2}} \approx \frac{1}{2} \frac{1}{(\pi\alpha)^{1/2}} C \ln \phi. \quad (3.114)$$

A comparison of (3.113) and (3.114) yields

$$\gamma_0 = \pi - \frac{C}{2} \left(\frac{\pi}{\alpha} \right)^{1/2}. \quad (3.115)$$

Thus we have matched the solution (3.110), (3.111) with a local solution corresponding to a flow in a corner of angle γ_0 (cf. Figure 3.6).

The value of θ at the separation point is

$$\theta = \theta_0 - \frac{C}{2} \left(\frac{\pi}{\alpha} \right)^{1/2}. \quad (3.116)$$

If we denote by β the angle between the wall and the free surface at E (see Figure 3.24) then (3.116) implies that

$$\beta = -\frac{C}{2} \left(\frac{\pi}{\alpha} \right)^{1/2}. \quad (3.117)$$

For the particular flow of Figure 3.24, (3.102) and (3.116) yield

$$\beta \approx \frac{\pi}{2\alpha^{1/2}} \quad \text{as } \alpha \rightarrow \infty. \quad (3.118)$$

We now present fully nonlinear solutions for arbitrary values of α . The presence of surface tension changes drastically the dynamic boundary condition and invalidates the techniques used for streamline flows. Exact solutions can no longer be expected and fully nonlinear solutions have to be calculated numerically. There are, however, a few examples of exact solutions. Those will be considered in Section 6.5.1.

We can calculate nonlinear solutions for the flow configuration of Figure 3.1 by modifying appropriately the series representation (3.35) to accommodate the singularity at $t = -1$. Using insight given by the asymptotic result (3.117), we assume that the flow near $t = -1$ is a flow in an angle $\pi + \beta$. Using (3.19) and (3.90) we obtain

$$w \sim f^{-\beta/\pi} \quad \text{as } \phi \rightarrow 0 \quad (3.119)$$

and

$$w \sim (t+1)^{-2\beta/\pi} \quad \text{as } t \rightarrow -1. \quad (3.120)$$

Therefore

$$w = (t-d)^{(\gamma_2-\gamma_1)/\pi} t^{\gamma_1/\pi} (t+1)^{-2\beta/\pi} \sum_{n=0}^{\infty} a_n t^n \quad (3.121)$$

is the appropriate generalisation of (3.35) when surface tension is included. The asymptotic solution (3.117) for α large suggests that β should be found as part of the solution.

We now present explicit calculations in the particular case $\gamma_1 = \gamma_2 = \pi/2$. In other words we consider the flow configuration of Figure 3.24. Then the expression (3.121) becomes

$$w = t^{1/2}(t+1)^{-2\beta/\pi} \sum_{n=0}^{\infty} a_n t^n. \quad (3.122)$$

The dynamic boundary condition is given in dimensionless variables by (3.100), where α is defined in (3.99).

We truncate the infinite series in (3.122) after N terms and calculate the coefficients a_n , $n = 0, \dots, N-1$, and β by satisfying (3.100) at the $N+1$ equally spaced mesh points

$$\sigma_I = \frac{\pi}{N+1} \left(I - \frac{1}{2} \right), \quad I = 1, \dots, N+1. \quad (3.123)$$

This leads to a system of $N+1$ equations with $N+1$ unknowns, which can be solved by Newton's method. We present numerical results in terms of the parameter

$$\alpha_v = 2\alpha. \quad (3.124)$$

The factor 2 in (3.124) has been introduced so that α_v coincides with the parameter α used by Vanden-Broeck [163].

Typical free surface profiles are shown in Figure 3.25. For $\alpha_v = \infty$, the free surface profile reduces to the free streamline solution of Figure 3.8. As $\alpha_v \rightarrow 0$, the free surface profile approaches the horizontal line $y = 1$ (i.e. the horizontal line through the stagnation point E). This is consistent with the fact that the dynamic boundary condition (3.100) predicts that the curvature of the free surface tends to zero as $\alpha_v \rightarrow 0$ (the straight line $y = 1$ has zero curvature).

Numerical values of β versus α_v are shown in Figure 3.26. As α_v varies from 0 to ∞ , β varies continuously from $\pi/2$ to 0. For $\alpha = \infty$, the dynamic boundary condition (3.100) reduces to the free streamline condition $u^2 + v^2 = 1$. The solution is then given by

$$\beta = 0; \quad a_0 = 1, \quad a_n = 0, \quad n = 1, 2, \dots \quad (3.125)$$

Substituting (3.125) into (3.122) we obtain

$$w_\infty = t^{1/2}. \quad (3.126)$$

This is the free streamline solution (3.39). Here the subscript ∞ refers to the value of α_v .

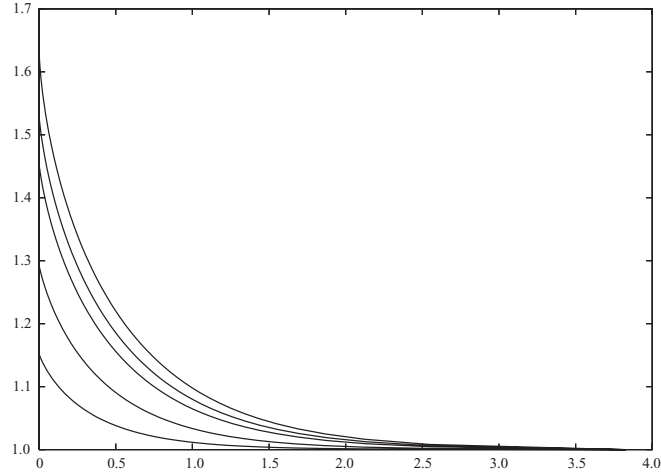


Fig. 3.25. Computed free surface profiles for the flow configuration of Figure 3.24. The profiles from top to bottom correspond to $\alpha_v = \infty$, $\alpha_v = 50$, $\alpha_v = 25$, $\alpha_v = 10$ and $\alpha_v = 5$; α_v is defined by (3.99) and (3.124).

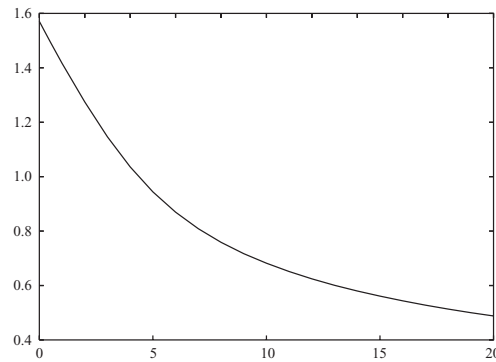


Fig. 3.26. Values of the angle β between the free surface and the wall at the separation point E (see Figure 3.24) versus α_v .

As $\alpha_v \rightarrow 0$, the free surface approaches a horizontal straight line. The solution is then

$$\beta = \frac{\pi}{2}, \quad a_0 = 2; \quad a_n = 0, \quad n = 1, 2, 3, \dots \quad (3.127)$$

Substituting (3.127) into (3.122) we obtain the following exact solution:

$$w_0 = \frac{2t^{1/2}}{t+1}. \quad (3.128)$$

Again the subscript 0 refers to the value of α_v .

As in Section 3.1.1, we can define the contraction ratio C_c as the ratio of the ordinate of the free surface as $x \rightarrow \infty$ and the ordinate of the separation point E .

For $\alpha_v = \infty$, we have

$$C_{c\infty} = \frac{\pi}{\pi + 2}. \quad (3.129)$$

(see (3.42)–(3.44) for an explicit derivation).

For $\alpha_v = 0$, the free surface is the horizontal line $y = 1$ and the ordinates of E and of the level of the free surface as $x \rightarrow \infty$ are equal to 1. Therefore

$$C_{c0} = 1. \quad (3.130)$$

In Figure 3.27 we present numerical values of C_c versus α_v . As α_v decreases from infinity, the contraction ratio increases monotonically from $C_{c\infty}$ to C_{c0} .

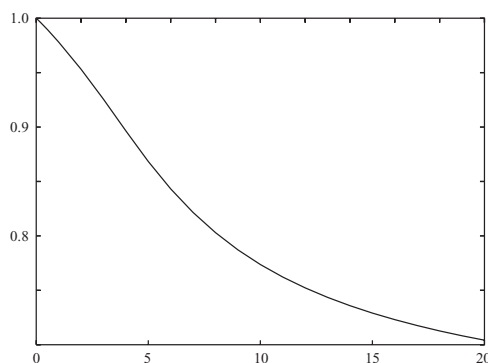


Fig. 3.27. Values of the contraction ratio C_c versus α_v for the flow configuration of Figure 3.24.

As $\alpha_v \rightarrow \infty$, the values of β are described by the asymptotic formula (3.117). Combining (3.117) and (3.124) we obtain

$$\beta \approx \frac{\pi}{(2\alpha_v)^{1/2}} \quad \text{as } \alpha_v \rightarrow \infty. \quad (3.131)$$

The numerical values in Figure 3.26 are in good agreement with (3.131) for α_v large. For $\alpha_v = 20$, the value of β predicted by (3.131) agrees with the numerical results within two per cent.

We can also construct a perturbation solution for α_v small by writing

$$\tau = \tau_0 + \alpha_v \tau_1 + O(\alpha^2), \quad (3.132)$$

$$\theta = \theta_0 + \alpha_v \theta_1 + O(\alpha^2). \quad (3.133)$$

Here τ_0 and θ_0 are defined by

$$\tau_0 - i\theta_0 = \ln w_0, \quad (3.134)$$

where w_0 is given by (3.128). Representing the free surface EF by (3.9), we find from (3.134) that

$$\tau_0 = -\ln \cos \frac{\sigma}{2}, \quad \theta_0 = 0, \quad 0 < \sigma < \pi, \quad (3.135)$$

on the free surface EF . Substituting (3.132) and (3.133) into (3.100) and equating coefficients of α_v , we obtain

$$\frac{\partial \theta_1}{\partial \phi} = \frac{1 \sin^2(\sigma/2)}{2 \cos(\sigma/2)}. \quad (3.136)$$

Using (3.10) and the chain rule we can rewrite (3.136) as

$$\frac{d\theta_1}{d\sigma} = -\frac{1}{2\pi} \sin \frac{\sigma}{2}. \quad (3.137)$$

Integrating (3.137) and using the condition $\theta_1 = 0$ at $\sigma = 0$, we obtain

$$\theta_1 = \frac{1}{\pi} \left(\cos \frac{\sigma}{2} - 1 \right). \quad (3.138)$$

In particular, (3.138) implies that

$$\theta_1 = -\frac{1}{\pi} \quad \text{at} \quad \sigma = \pi. \quad (3.139)$$

Combining (3.117), (3.133) and (3.139) we obtain

$$\beta = \frac{\pi}{2} - \frac{\alpha_v}{2\pi} \quad \text{as} \quad \alpha_v \rightarrow 0. \quad (3.140)$$

For $\alpha_v = 1$, the value of β predicted by (3.140) agrees with the numerical results within two per cent.

3.2.2 Free separation

The behaviour (3.94) occurs for all free streamline problems near the intersection of a free surface with a rigid wall. The constant S depends on the geometry of the problem. When $S > 0$, as in the flow of Figure 3.24, there is locally a flow around a corner near the separation point E (see (3.93),

(3.101), (3.102) and (3.118)). The velocity at the separation point E then becomes infinite when surface tension is included. An interesting question is whether there are free streamline flows for which $S \leq 0$. Of particular interest are flows for which $S = 0$ and therefore for which the singular behaviour (3.94) disappears. For $S < 0$, the asymptotic analysis of the previous section suggests that, when surface tension is included, the flow near the separation point is a flow inside an angle with a stagnation point at the separation. In this section we will show that there are free streamline flows with $S \leq 0$ when the rigid boundaries are curved. The consideration of such flows will enable us to introduce the concept of selection, which will be very useful when we are studying gravity–capillary flows.

We consider the open-cavity model of Figure 3.16 but now with the effect of the surface tension T included in the dynamic boundary condition. Proceeding as in Section 3.1.2 we seek $\tau - i\theta$ as an analytic function of $\phi + i\psi$ in the lower half-plane, $\psi < 0$, of the domain shown in Figure 3.17. This function must satisfy (3.50), (3.51) and

$$-\frac{e^\tau}{b} \frac{\partial \theta}{\partial \phi} = \frac{\alpha}{2}(e^{2\tau} - 1) \quad \text{on } \psi = 0, \quad 1 < \phi < \infty. \quad (3.141)$$

Here α is defined by

$$\alpha = \frac{\rho U^2 R}{T}. \quad (3.142)$$

We start our investigation by reconsidering the solutions of Section 3.1.2 and by calculating the curvature K_A of the free surface at the separation point A . Using (3.49) and (3.62), we find that

$$K_A = \frac{1}{b} \frac{\partial \theta}{\partial \phi} \approx -\frac{1}{2} C (b\phi - b)^{-1/2} \quad \text{as } \phi \rightarrow 1, \quad (3.143)$$

where

$$C = -b^{-1/2} - b^{-1/2} \sum_{n=1}^{\infty} (-1)^{n+1} (2n-1) A_n. \quad (3.144)$$

Since the A_n are functions of γ , (3.144) defines C as a function of $\bar{\gamma}$. A graph of C versus the angular position $\bar{\gamma}$ of the separation points is shown in Figure 3.28. If the angle β is counted positive when shown as in Figure 3.16, a comparison of Figures 3.24 and 3.16 shows that (3.117) implies that

$$\beta = \frac{C}{2} \left(\frac{\pi}{\alpha} \right)^{1/2}. \quad (3.145)$$

In other words β has opposite signs in Figures 3.16 and 3.24. This

difference in sign has been maintained to be consistent with previously published results.

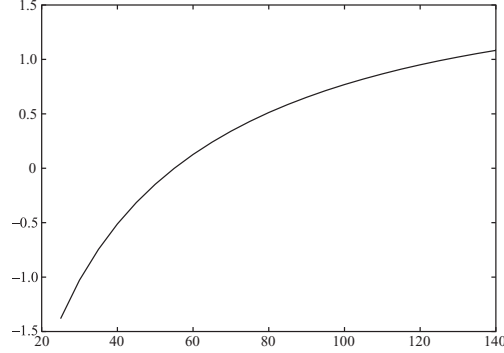


Fig. 3.28. Values of the constant C versus $\bar{\gamma}$.

The constant C vanishes when $\bar{\gamma} = \gamma^* \approx 55^\circ$ (see Figure 3.28). Thus (3.143) shows that the curvature of the free surface at the separation points is infinite unless $\bar{\gamma} = \gamma^*$.

For $\bar{\gamma} > \gamma^*$, Figure 3.28 shows that $C > 0$ and (3.145) predicts $\beta > 0$. The flow near B in Figure 3.16 is a flow inside an angle with zero velocity at B . For $\bar{\gamma} < \gamma^*$, Figure 3.28 shows that $C < 0$ and the values of β predicted by (3.145) are then negative. The flow near B is then a flow around a corner with infinite velocity at B . These results are only valid for α large. As $\alpha \rightarrow 0$, (3.141) shows that the curvature of the free surfaces tends to zero. Since the flows are characterised by a constant velocity at infinity, the free surfaces must approach two horizontal straight lines. Therefore

$$\beta \rightarrow \gamma - \frac{\pi}{2} \quad \text{as } \alpha \rightarrow 0. \quad (3.146)$$

Relation (3.146) shows that $\beta < 0$ in the limit $\alpha \rightarrow 0$ when $\bar{\gamma} < \pi/2$. Relation (3.145) shows that $\beta > 0$ in the limit $\alpha \rightarrow \infty$ when $\bar{\gamma} > \gamma^*$. If we assume that, for a given value of $\bar{\gamma}$, β is a continuous function of α then there must exist for each value of α a particular value of $\gamma^* < \bar{\gamma} < \pi/2$ for which $\beta = 0$ (i.e. for which the flow leaves the circle tangentially). We describe these particular values of $\bar{\gamma}$ by the function

$$\bar{\gamma} = g(\alpha). \quad (3.147)$$

This conjecture is confirmed by the nonlinear computations below. In

particular these results show that

$$g(\alpha) \rightarrow \gamma^* \quad \text{as } \alpha \rightarrow \infty. \quad (3.148)$$

This implies that the limit $T \rightarrow 0$ can be used to select a particular solution with $T = 0$. In Section 3.1.2 we calculated solutions for $T = 0$. Then the dynamic boundary condition implies $\beta = 0$. We obtained solutions for all values of $\bar{\gamma}$. When $T \neq 0$, solutions with $\beta = 0$ exist only for values of $\bar{\gamma}$ satisfying (3.147). Taking the limit $\alpha \rightarrow \infty$, (3.146) shows that we should select the solution corresponding to $\bar{\gamma} = \gamma^*$, which is known as the one satisfying the Brillouin–Villat condition (see [22], [194], [19] and [69]). This condition was introduced to select the position of the separation points in the case of free separation without surface tension. It requires the pressure to be minimal in the cavity. By Bernoulli's equation (3.1), this is equivalent to the condition that the velocity is a maximum on the free streamlines. For the configuration of Figure 3.16, the Brillouin–Villat condition yields $\bar{\gamma} = \gamma^*$.

The above analysis shows that the selection mechanism based on the limit $T \rightarrow 0$ provides a new physical interpretation of the Brillouin–Villat condition.

We will now solve the problem numerically, calculate $g(\alpha)$ and demonstrate (3.148). We first map the flow of Figure 3.16 into the unit circle in the t -plane by the transformation

$$t = \frac{1 + if^{1/2}}{1 - if^{1/2}}. \quad (3.149)$$

The flow configuration in the t -plane is shown in Figure 3.29.

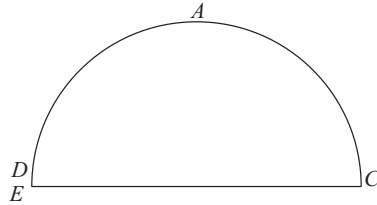


Fig. 3.29. The flow configuration of Figure 3.16 in the t -plane defined by (3.149).

Next we note that the flow near A is locally a flow inside a corner with angle $\pi - \beta$ and that the flow near C is a flow inside a right-angle corner (see Figure 3.16). Therefore, using (3.149), we obtain

$$u - iv \sim (t - i)^{\beta/\pi} \quad \text{as } t \rightarrow i, \quad (3.150)$$

$$u - iv \sim t - 1 \quad \text{as } t \rightarrow 1. \quad (3.151)$$

Following the series truncation method of Section 3.1.2, we represent the complex velocity by

$$u - iv = e^{\tau - i\theta} = (1 - t)(1 + t^2)^{\beta/\pi} \sum_{n=0}^{\infty} a_n t^n. \quad (3.152)$$

The multiplicative factors in front of the series in (3.152) remove the singularity (3.150). Therefore we can expect the series in (3.152) to converge in the unit circle of the t -plane.

If we describe points on the unit circle by $t = e^{i\sigma}$, $0 < \sigma < \pi$, we can rewrite (3.141) and (3.51) as

$$-\frac{e^\tau \cos^3(\sigma/2)}{b \sin(\sigma/2)} \frac{d\theta}{d\sigma} = \frac{\alpha}{2} (e^{2\tau} - 1), \quad \frac{\pi}{2} < \sigma < \pi, \quad (3.153)$$

$$\frac{e^\tau \cos^3(\sigma/2)}{b \sin(\sigma/2)} \frac{d\theta}{d\sigma} = 1, \quad 0 < \sigma < \frac{\pi}{2}. \quad (3.154)$$

Coefficients a_n in (3.152) are found such that (3.153) and (3.154) are satisfied. This is achieved by series truncation as in Section 3.1.2. We truncate the infinite series in (3.152) after N terms and find the N coefficients a_0, a_1, \dots, a_{N-1} , the constant b and the angle β by collocation. Thus we introduce the N mesh points

$$\sigma_I = \left(I - \frac{1}{2} \right) \frac{\pi}{N}, \quad I = 1, \dots, N. \quad (3.155)$$

In order to avoid the value $\sigma = \pi/2$ at which the expression (3.152) is singular, we choose N to be even. Using (3.152) and (3.155) we obtain $\tilde{\tau}(\sigma)$ and $\tilde{\theta}(\sigma)$ at the points σ_I in terms of the coefficients a_n . Substituting these expressions into (3.153) and (3.154) we obtain N equations. An extra equation is obtained by requiring the velocity to be unity at infinity. This leads to

$$\tilde{\tau}(\pi) = 0. \quad (3.156)$$

The last equation relates γ and the angle θ at the separation point:

$$\gamma + [\tilde{\theta}(\sigma)]_{\sigma=\pi/2} = \frac{\pi}{2}. \quad (3.157)$$

This system of $N + 1$ equations with $N + 1$ unknowns can be solved by Newton's method. We used this numerical scheme to compute solutions for various values of α and $\bar{\gamma}$. The coefficients a_n were found to decrease rapidly as n increases. For example, for $\gamma = 30^\circ$ and $\alpha = 10$, $a_1 \approx 0.6$,

$a_{10} \approx -0.3 \times 10^{-2}$ and $a_{40} \approx 0.3 \times 10^{-3}$. In Figure 3.30 we present numerical values of β/π versus $\bar{\gamma}$ for $\alpha = 1$.

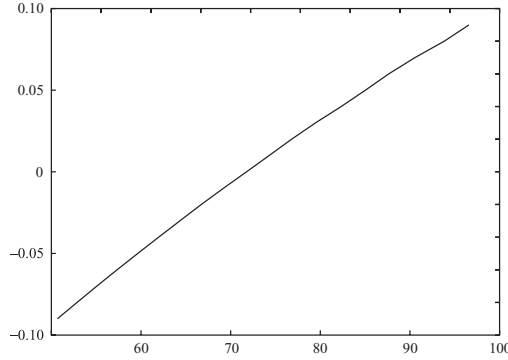


Fig. 3.30. Values of β/π versus $\bar{\gamma}$ (in degrees) for $\alpha = 1$.

The curve in Figure 3.30 shows that for $\alpha = 1$ there is exactly one value of $\bar{\gamma}$ at which $\beta = 0$. Similar results were found for other values of α (see [176] and [183]). As $\alpha \rightarrow 0$, the free surfaces in figure 3.16 approach two horizontal lines. Therefore the curve corresponding to $\alpha = 0$ in Figure 3.30 is the straight line (not shown in the figure) of equation

$$\beta = \bar{\gamma} - \frac{\pi}{2}. \quad (3.158)$$

For $\alpha = \infty$, the angle β is equal to zero for all values of $\bar{\gamma}$ and the curve corresponding to $\alpha = \infty$ in Figure 3.30 is the horizontal line $\bar{\gamma} = 0$ (not shown).

These results imply that, for each value of $\alpha \neq \infty$, there is a particular value $\bar{\gamma}$ for which $\beta = 0$ (i.e. for which the free surface leaves the obstacle tangentially). We denote these particular values of $\bar{\gamma}$ by the function (3.147). In Figure 3.31 we present computed values of $\bar{\gamma} = g(\alpha)$ versus α^{-1} . As $\alpha \rightarrow 0$, $\bar{\gamma} \rightarrow 90^\circ$. As $\alpha \rightarrow \infty$, $\bar{\gamma} \rightarrow \gamma^*$. Therefore the particular solution that satisfies the Brillouin–Villat condition in the absence of surface tension can be viewed as the limit of the family of solutions in Figure 3.31 as the surface tension approaches zero.

So far we have mainly considered solutions with $\beta = 0$. It is of interest to look at solutions with $\beta \neq 0$. The angle β can then be interpreted as a contact angle whose value depends on the properties of the fluid and of the rigid boundary. In Figure 3.32 we present values of $\bar{\gamma}$ versus α^{-1} for $\beta = 0.04\pi$.

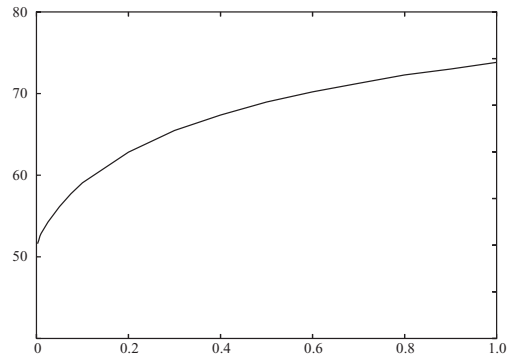


Fig. 3.31. Values of $\tilde{\gamma}$ versus α^{-1} . The corresponding free surface profiles leave the circular object tangentially, i.e. $\beta = 0$.

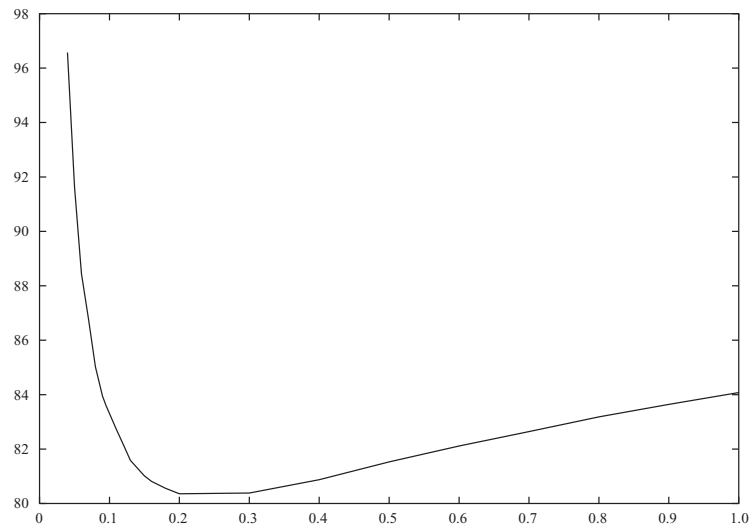


Fig. 3.32. Values of $\tilde{\gamma}$ versus α^{-1} for $\beta = 0.04\pi$.

This curve can be viewed as the equivalent of the curve (3.147) but with $\beta = 0.04\pi$ instead of $\beta = 0$. One interesting property to note in Figure 3.32 is that now $\tilde{\gamma}$ is not a monotonic function of α^{-1} . However, only one value of $\tilde{\gamma}$ corresponds to each value of the surface tension (i.e. α^{-1}). For α^{-1} small, $\tilde{\gamma}$ increases rapidly. This behaviour can be described by substituting $\beta = 0.04\pi$ into (3.145) and noting that

$$C = 2(0.04\pi) \left(\frac{\alpha}{\pi}\right)^{1/2}. \quad (3.159)$$

Together with Figure 3.28, this predicts that $\bar{\gamma}$ increases as α^{-1} decreases, for α large.

3.3 The effects of gravity

In this section we study solutions for the flow configuration of Figure 3.1 with surface tension neglected but with gravity included in the dynamic boundary condition. We assume that gravity acts in the direction defined by the angle β_1 (see Figure 3.33) and write the dynamic boundary condition as

$$\frac{1}{2}(u^2 + v^2) + gy \sin \beta_1 - gx \cos \beta_1 = B, \quad (3.160)$$

where B is the Bernoulli constant. In this section we will look for solutions without waves on EF . Solutions with waves on EF will be studied in Chapter 8.

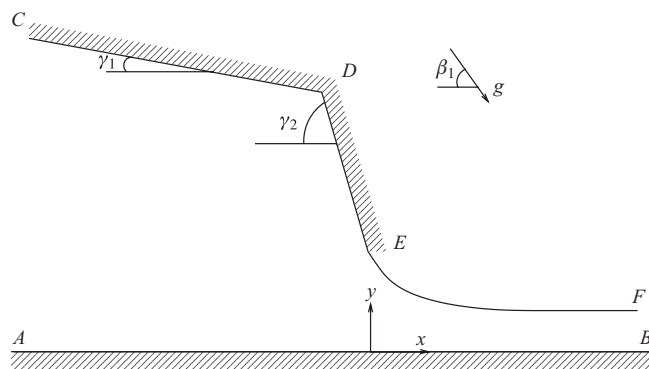


Fig. 3.33. The flow configuration of Figure 3.1 with the effects of gravity included.

Two situations of particular interest are $\beta_1 = \pi/2$ and $\beta_1 = 0$. When $\beta_1 = \pi/2$, gravity is acting in the negative y -direction. One interpretation of the flow of Figure 3.33 is then the flow emerging from a container with gravity included. Another is the flow under a sluice gate, a classical topic in hydraulics (see [11], [54], Larock [93], Chung [30], Vanden-Broeck [181] and Binder and Vanden-Broeck [15], [16]).

There are now two free surfaces CD and EF (see Figure 3.34). The model consists of replacing the upper free surface CD by a rigid lid (see Figure 3.35). The configuration of Figure 3.35 is that of Figure 3.33 with $\gamma_1 = 0$. An accurate numerical study of the complete free surface flow of Figure 3.34 is presented in Section 8.3.

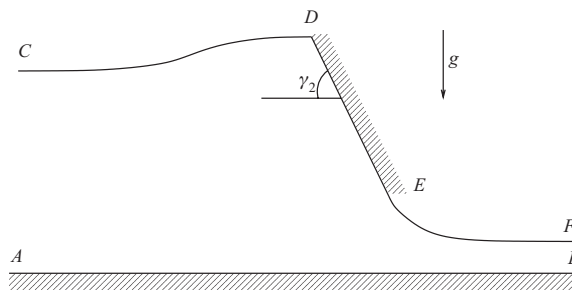
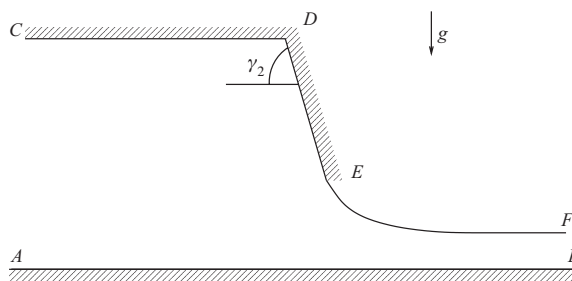


Fig. 3.34. A free surface flow under a sluice gate.

Fig. 3.35. A model for the flow under a sluice gate, in which the free surface CD has been replaced by a rigid lid.

When $\beta_1 = 0$, gravity is acting in the positive x -direction. A realistic view of the flow is obtained by rotating Figure 3.33 by 90° clockwise. If the flow is then reflected in the wall AB , the result corresponds to a jet falling from a nozzle (see Figure 3.36).

In Figures 3.33 and 3.36 we have assumed that the free surface EF leaves the wall DE tangentially. As we shall see, there are in addition solutions for which EF does not leave the wall DE tangentially.

There is then an angle μ between the wall DE and the free surface EF at the separation point E (see Figure 3.37). There are only three possible values for μ . One of them is $\mu = \pi$; it corresponds to the case already mentioned where the free surface leaves the wall tangentially. The existence of these three values of μ is to be contrasted with the problems including surface tension discussed in Section 3.2, where all values of μ were in principle possible, and with the free streamline problems in Section 3.1, where only the value $\mu = \pi$ was acceptable.

The existence of the two values of $\mu \neq \pi$ can be established by deriving a local solution valid in the neighbourhood of the separation point E . The

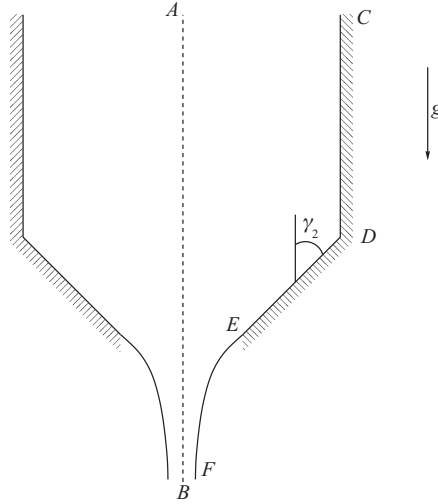


Fig. 3.36. The free surface flow emerging from a nozzle. This is the flow configuration of Figure 3.33 rotated by 90° and reflected in the wall AB . Here $\gamma_1 = 0$ and $\beta_1 = 0$.

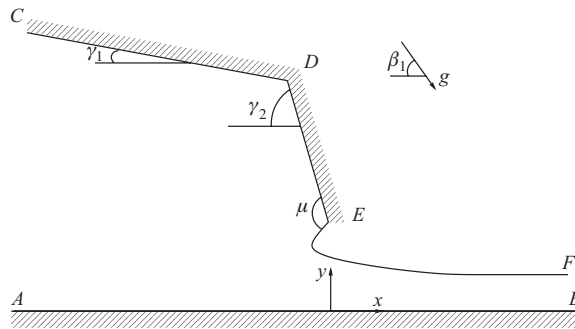


Fig. 3.37. The flow of Figure 3.33 with an angle μ between the free surface and the wall at the separation point E .

analysis follows the work of Dagan and Tulin [40]. We define new local coordinates x and y with the origin at the separation point and such that gravity is acting in the negative y -direction. The local flow is illustrated in Figure 3.38. Here the separation point is denoted by G , the wall by HG and the free surface by GL . It can easily be seen that the flow of Figure 3.38 describes the flow near E in Figure 3.37 if

$$\mu_2 = \frac{\pi}{2} - \beta_1 + \gamma_2. \tag{3.161}$$

If $\mu = \pi$, the free surface LG leaves the wall HG tangentially and the velocity at G is finite and different from zero. If $\mu < \pi$, the flow is locally a flow inside a corner and the velocity at G is zero (i.e. G is a stagnation point). If $\mu > \pi$, the flow is locally a flow around a corner and the velocity at G is infinite (see Figure 3.6 and (3.19)). Therefore values of $\mu > \pi$ are not possible, since (3.160) requires the velocity at G to be finite.

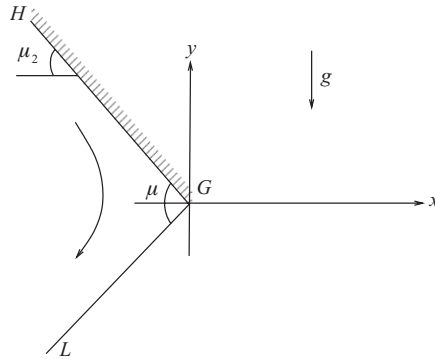


Fig. 3.38. Local-gravity free surface flow near the intersection of a wall HG with a free surface GL .

We shall now determine the allowed values of μ when $\mu < \pi$. We define a potential function ϕ and a streamfunction ψ and choose $\phi = \psi = 0$ at the point G . The complex potential plane is shown in Figure 3.39.

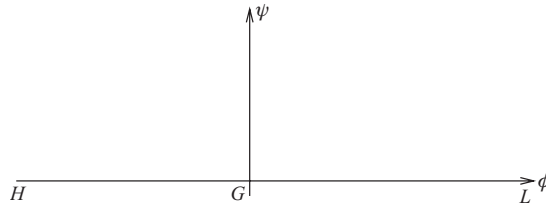


Fig. 3.39. The flow of Figure 3.38 in the complex potential plane. The flow domain is $\psi < 0$.

Using (3.17) we express the local solution in the form

$$z = Af^{\mu/\pi}. \quad (3.162)$$

We write the complex constant A as

$$A = ae^{i\alpha}, \quad (3.163)$$

where a and α are real and α is such that the kinematic boundary condition on the wall HG is satisfied. On the wall HG , $\arg z = \pi - \mu_2$. However, the argument of (3.162) evaluated on $\psi = 0$, $\phi < 0$, gives $\arg z = -\mu + \alpha$. Equating the two expressions for $\arg z$ gives

$$\alpha = \pi + \mu - \mu_2. \quad (3.164)$$

Substituting (3.163) and (3.164) into (3.162) yields

$$z = af^{\mu/\pi} e^{i(\pi + \mu - \mu_2)}. \quad (3.165)$$

Before satisfying the dynamic boundary condition we need to improve the local solution (3.165) by writing explicitly the next-order correction:

$$z = af^{\mu/\pi} e^{i(\pi + \mu - \mu_2)} + bf^\nu e^{i\delta} + \dots \quad (3.166)$$

Here ν , b and δ are real constants. The second term in (3.166) takes into account the deviation of the free surface from the straight line GL as ϕ increases. Since we require the second term in (3.166) to be a small correction to (3.165) in the limit $f \rightarrow 0$, we impose

$$\nu > \frac{\mu}{\pi}. \quad (3.167)$$

Taking the real and imaginary parts of (3.166) on $\psi = 0$, $\phi > 0$, we obtain

$$x = a\phi^{\mu/\pi} \cos(\pi + \mu - \mu_2) + b\phi^\nu \cos \delta + \dots, \quad (3.168)$$

$$y = a\phi^{\mu/\pi} \sin(\pi + \mu - \mu_2) + b\phi^\nu \sin \delta + \dots. \quad (3.169)$$

Differentiating (3.168) and (3.169) with respect to ϕ yields

$$\begin{aligned} x_\phi^2 + y_\phi^2 &= \left(\frac{a\mu}{\pi}\right)^2 \phi^{2\mu/\pi-2} + 2\frac{a\mu}{\pi} b\nu \phi^{\mu/\pi+\nu-2} \\ &\quad \times \cos(\pi + \mu - \mu_2 - \delta) + b^2 \nu^2 \phi^{2\nu-2} + \dots. \end{aligned} \quad (3.170)$$

Since

$$\frac{2\mu}{\pi} - 2 < \frac{\mu}{\pi} + \nu - 2 < 2\nu - 2, \quad (3.171)$$

the last term in (3.170) is of lower order and can be neglected. We can rewrite (3.170) as

$$x_\phi^2 + y_\phi^2 = \left(\frac{a\mu}{\pi}\right)^2 \phi^{2\mu/\pi-2} \left[1 + \frac{2\pi}{a\mu} b\nu \phi^{\nu-\mu/\pi} \cos(\pi + \mu - \mu_2 - \delta) \right] + \dots \quad (3.172)$$

and express $u^2 + v^2$ in the limit $f \rightarrow 0$ as

$$\begin{aligned} u^2 + v^2 &= \frac{1}{x_\phi^2 + y_\phi^2} \\ &= \left(\frac{\pi}{a\mu}\right)^2 \phi^{2-2\mu/\pi} \left[1 - \frac{2\pi}{a\mu} b\nu\phi^{\nu-\mu/\pi} \cos(\pi + \mu - \mu_2 + \delta)\right] + \dots. \end{aligned} \quad (3.173)$$

We now substitute (3.169) and (3.173) into the dynamic boundary condition (3.160). First we note that $\beta_1 = \pi/2$ since g is acting in the negative y -direction in Figure 3.38 and that $B = 0$ since $u = v = 0$ at the point G . This gives

$$\frac{1}{2} \left(\frac{\pi}{a\mu}\right)^2 \phi^{2-2\mu/\pi} + ga\phi^{\mu/\pi} \sin(\pi + \mu - \mu_2) + gb\phi^\nu \sin \delta + \dots = 0. \quad (3.174)$$

We then equate the coefficients of the leading-order terms in (3.174). If $\pi + \mu - \mu_2 \neq \pi$ then the first and second terms in (3.174) give

$$\frac{\mu}{\pi} = 2 - \frac{2\mu}{\pi} \quad \text{or} \quad \mu = \frac{2\pi}{3} \quad (3.175)$$

and

$$a = \left[\frac{1}{2} \frac{\pi^2}{\mu^2} \frac{1}{g \sin(\mu_2 - \mu - \pi)} \right]^{1/3}. \quad (3.176)$$

Since $\mu = 2\pi/3$, we require $-\pi/3 < \mu_2 < 2\pi/3$, for otherwise the free surface in Figure 3.38 would descend towards the stagnation point G and this would be in contradiction with the dynamic boundary condition (3.160) with $\beta_1 = \pi/2$, which implies that a stagnation point on a free surface is the highest point on it. In the remaining part of this chapter we will assume $\mu_2 > 0$; however, solutions with $\mu_2 < 0$ will be considered in Chapter 8 (see Figure 8.5, where $\gamma_3 = -\mu_2$). Furthermore, the solution with $\mu_2 = -\pi/6$ will be used in Section 6.5.2 to describe the singularity near the crests of the highest gravity waves. If

$$\pi + \mu - \mu_2 = \pi \quad \text{or} \quad \mu = \mu_2, \quad (3.177)$$

the second term in (3.174) vanishes and the balance of the remaining terms gives

$$\nu = 2 - \frac{2\mu}{\pi}. \quad (3.178)$$

The conditions (3.167), (3.177) and (3.178) yield

$$\mu = \mu_2 < \frac{2\pi}{3}. \quad (3.179)$$

The condition (3.177) implies that the free surface LG is horizontal.

In summary we have the following possibilities. If $\mu_2 \leq 2\pi/3$, there are three possible values for μ : π , $2\pi/3$ and μ_2 . However, if $\mu_2 \geq 2\pi/3$ then the only possible value for μ is π .

We note that on the one hand the solution (3.162) with $\mu = 2\pi/3$ and A defined by (3.163), (3.164) and (3.176) is an exact solution for the flow configuration of Figure 3.38 for all values of z inside the angle HGL . On the other hand the solution (3.162) with $\mu = \mu_2$ is only a local solution in the limit $z \rightarrow 0$.

We shall solve the flow problem of Figure 3.37 numerically by using a series truncation method similar to that used in Section 3.2. All the solutions constructed in this section are waveless as $x \rightarrow \infty$. Solutions with waves as $x \rightarrow \infty$ will be computed in Chapter 8. The flow configuration in the complex potential plane is shown in Figure 3.4. As in Section 3.1.1, we map the complex potential plane onto the inside of the unit circle in the t -plane by using the transformation (3.8). The flow configuration in the t -plane is illustrated in Figure 3.5. Next we represent the complex velocity $w = u - iv$ by the expansion (3.12) where $G(t)$ contains all the singularities of w in $|t| \leq 1$. In this case there are two singularities: one is at the separation point E and the other at $t = 1$ (i.e. as $x \rightarrow \infty$).

The former corresponds to a flow inside an angle μ (see Figure 3.37) and is described by

$$w \approx f^{1-\mu/\pi} \quad \text{as } f \rightarrow 0 \quad (3.180)$$

(see (3.19)). Using (3.8) we have

$$w \approx (1+t)^{2-2\mu/\pi} \quad \text{as } t \rightarrow -1. \quad (3.181)$$

The singularity at $t = 1$ depends on the value of β_1 . It can be seen from (3.160) that

$$u^2 + v^2 \approx 2gx \cos \beta_1 \quad \text{as } x \rightarrow \infty \quad \text{when } \beta_1 \neq \pi/2 \quad (3.182)$$

and that

$$u^2 + v^2 \approx \text{constant} \quad \text{as } x \rightarrow \infty \quad \text{when } \beta_1 = \pi/2. \quad (3.183)$$

In (3.183) we have used the fact that there are no waves as $x \rightarrow \infty$.

We first examine the case $\beta \neq \pi/2$ (see Figure 3.37). Relation (3.182) shows that $u^2 + v^2 \rightarrow \infty$ as $x \rightarrow \infty$. Since the flux between the free surface EF and the wall AB is finite (and equal to Q), it follows by conservation of mass that the free surface approaches the wall asymptotically as $x \rightarrow \infty$.

In other words the flow reduces to an arbitrarily thin jet in the x -direction as $x \rightarrow \infty$. Therefore $u \gg v$ as $x \rightarrow \infty$, and (3.182) implies that

$$u \approx (2gx \cos \beta_1)^{1/2}. \quad (3.184)$$

If we denote by $y = \eta(x)$ the equation of the free surface then from the conservation of mass we have

$$u\eta(x) = Q. \quad (3.185)$$

Combining (3.184) and (3.185) we have

$$\eta(x) \approx Q(2gx \cos \beta)^{-1/2}. \quad (3.186)$$

Writing successively ϕ_x and ψ_y for u in (3.184) gives

$$\frac{\partial \phi}{\partial x} = (2gx \cos \beta)^{1/2}, \quad (3.187)$$

$$\frac{\partial \psi}{\partial y} = (2gx \cos \beta)^{1/2}. \quad (3.188)$$

Integrating (3.187) with respect to x and (3.188) with respect to y gives expressions for ϕ and ψ . Combining them gives

$$f = \phi + i\psi = (2g \cos \beta_1)^{1/2} \left(\frac{2}{3}x^{3/2} + ix^{1/2}y \right). \quad (3.189)$$

We note that, for x large,

$$z^{3/2} = x^{3/2} \left(1 + \frac{iy}{x} \right)^{3/2} \approx x^{3/2} \left(1 + i\frac{3y}{2x} \right) = x^{3/2} + i\frac{3x^{1/2}y}{2}. \quad (3.190)$$

Combining (3.189) and (3.190) gives

$$f \sim z^{3/2} \quad \text{or} \quad z \sim f^{2/3}. \quad (3.191)$$

Differentiating (3.191) with respect to z and eliminating z by using the second of the relations (3.191) yields

$$\frac{df}{dz} = u - iv \sim z^{1/2} \sim f^{1/3}. \quad (3.192)$$

Next we examine the case $\beta_1 = \pi/2$ (see Figure 3.37). Then the flow approaches a uniform stream with constant velocity U and constant depth H as $x \rightarrow \infty$ (see (3.183)). The exact equations that describe the flow as

$x \rightarrow \infty$ are, in dimensional variables,

$$\phi_{xx} + \phi_{yy} = 0, \quad 0 < y < H + \eta(x), \quad (3.193)$$

$$\phi_y = \phi_x \eta_x \quad \text{on} \quad y = H + \eta(x), \quad (3.194)$$

$$\frac{1}{2}(\phi_x^2 + \phi_y^2) + gy = \frac{1}{2}U^2 + gH \quad \text{on} \quad y = H + \eta(x), \quad (3.195)$$

$$\phi_y = 0 \quad \text{on} \quad y = 0. \quad (3.196)$$

Here $y = H + \eta(x)$ is the equation of the free surface. Equations (3.194) and (3.196) are the kinematic boundary conditions on the free surface and on the bottom, and equation (3.195) is the dynamic boundary condition on the free surface.

We write

$$w = U + \tilde{w} + \dots, \quad (3.197)$$

$$\phi = Ux + \tilde{\phi} + \dots, \quad (3.198)$$

$$\eta = \tilde{\eta} + \dots, \quad (3.199)$$

where \tilde{w} , $\tilde{\phi}$ and $\tilde{\eta}$ are assumed to be small perturbations. We have assumed as before that the flow approaches a uniform stream as $x \rightarrow \infty$. Substituting (3.197)–(3.199) into (3.193)–(3.196) and linearising yields

$$\tilde{\phi}_{xx} + \tilde{\phi}_{yy} = 0, \quad (3.200)$$

$$U\tilde{\eta}_x = \tilde{\phi}_y \quad \text{on} \quad y = H, \quad (3.201)$$

$$U\tilde{\phi}_x + g\tilde{\eta} = 0 \quad \text{on} \quad y = H, \quad (3.202)$$

$$\tilde{\phi}_y = 0 \quad \text{on} \quad y = 0. \quad (3.203)$$

Eliminating η between (3.201) and (3.202) gives

$$U\tilde{\phi}_{xx} + \frac{g}{U}\tilde{\phi}_y = 0 \quad \text{on} \quad y = H. \quad (3.204)$$

We use separation of variables, to find a solution of (3.200) in the form

$$\tilde{\phi}(x, y) = X(x)Y(y). \quad (3.205)$$

Substituting (3.205) in (3.200) and in (3.203) yields the ordinary differential equations

$$\frac{X''(x)}{X(x)} = -\frac{Y''(y)}{Y(y)} = \tilde{\mu}^2 \quad (3.206)$$

and the boundary condition

$$Y'(0) = 0. \quad (3.207)$$

Here $\tilde{\mu}^2$ is the separation constant. The solutions of the two differential equations (3.206) satisfying (3.207) are

$$X(x) = Be^{-\tilde{\mu}x} + Ce^{\tilde{\mu}x}, \quad (3.208)$$

$$Y(y) = D \cos \tilde{\mu}y, \quad (3.209)$$

where B , C and D are constants. We set $C = 0$, so that $\tilde{\phi}$ remains bounded as $x \rightarrow \infty$. Multiplying (3.208) and (3.209) yields the solution

$$\tilde{\phi} = Ae^{-\tilde{\mu}x} \cos \tilde{\mu}y, \quad (3.210)$$

where $A = DB$ is a constant. Substituting (3.210) into (3.204) yields

$$\tilde{\mu}H = \frac{1}{F^2} \tan \tilde{\mu}H, \quad (3.211)$$

where

$$F = \frac{U}{(gH)^{1/2}} \quad (3.212)$$

is the Froude number. We note that the derivation leading to (3.210) is similar to that leading to (2.74) and (2.75) in the theory of linear waves. The main difference is that we chose a negative separation constant in (2.72) whereas we have chosen a positive one in (3.206).

Substituting (3.210) into (3.198) and differentiating with respect to x gives

$$w = \frac{\partial \phi}{\partial x} - i \frac{\partial \phi}{\partial y} = U - A\tilde{\mu}e^{-\tilde{\mu}z}. \quad (3.213)$$

Next we rewrite (3.213) in terms of t . Using (3.8) we obtain, as $z \rightarrow \infty$ or equivalently as $t \rightarrow 1$,

$$e^{-f} \approx (1-t)^{2/\pi} \quad \text{as } t \rightarrow 1. \quad (3.214)$$

Combining (3.213) and (3.214) and using the dimensionless variables $U = 1$, $H = 1$, we have

$$w \approx 1 - A\tilde{\mu}(1-t)^{2\tilde{\mu}/\pi} \quad \text{as } t \rightarrow 1. \quad (3.215)$$

Similarly (3.211) gives in dimensionless variables

$$\tilde{\mu} = \frac{1}{F^2} \tan \tilde{\mu}. \quad (3.216)$$

Relations (3.215) and (3.216) define the singular behaviour of w as $t \rightarrow 1$ for $\beta_1 = \pi/2$.

Finally we use (3.214) to rewrite (3.192) as

$$w \approx [-\ln(1-t)]^{1/3} \quad \text{as } t \rightarrow 1. \quad (3.217)$$

This demonstrates the singular behaviour of w as $t \rightarrow 1$ when $\beta \neq \pi/2$.

3.3.1 Solutions with $\beta_1 = 0$ (funnels)

We first consider the configuration of Figure 3.37 with $\beta_1 = 0$. Following the approach of Sections 3.1.1 and 3.2, we find that the complex velocity w is represented by the expression

$$w = \left(\frac{t-d}{1-td} \right)^{(\gamma_2-\gamma_1)/\pi} t^{\gamma_1/\pi} \frac{[-\ln C_p(1-t)]^{1/3}}{(-\ln C_p)^{1/3}} (1+t)^{2-2\mu/\pi} \bar{G}(t), \quad (3.218)$$

where t is defined by (3.8). Here C_p is an arbitrary constant. The various factors appearing in the numerator of the expression multiplying $\bar{G}(t)$ remove the singularities in w at $t = 0$ (see (3.33)), $t = 1$ (see (3.217)), $t = d$ (see (3.27)) and $t = -1$ (see (3.181)). The factors appearing in the denominator of the expression multiplying $\bar{G}(t)$ are not essential and the computations could have been performed without them. The function $\bar{G}(t)$ in (3.218) is then free of singularities and can be written as the Taylor expansion

$$\bar{G}(t) = \sum_{n=0}^{\infty} a_n t^n. \quad (3.219)$$

There are of course alternative representations for $\bar{G}(t)$. For example we shall see in Section 3.3.2 that another convenient representation for $\bar{G}(t)$ is

$$\bar{G}(t) = \exp \left(\sum_{n=0}^{\infty} a_n t^n \right) \quad (3.220)$$

(see also (3.60)). We choose $0 < C_p < 0.5$ in (3.218), so that

$$[-\ln C_p(1-t)]^{1/3}$$

is real for $-1 < t < 1$. Then it can be easily checked that the kinematic boundary conditions on the walls CD , DE and AB are automatically satisfied by assuming that the coefficients a_n in (3.219) are real. For the computation presented we chose $C_p = 0.2$. We note that different values of C_p and different choices for $\bar{G}(t)$ (see (3.219) or (3.220)) will yield different values

for the coefficients a_n . However these various series representations yield the same values of w provided that, all the singularities in the unit circle of the complex t -plane have been properly removed.

We present explicit solutions for $\gamma_1 = \gamma_2 \neq 0$ (the analysis follows Lee and Vanden-Broeck [94]). After reflection in the wall AB , this models a jet of fluid emerging from a funnel (see Figure 3.40).

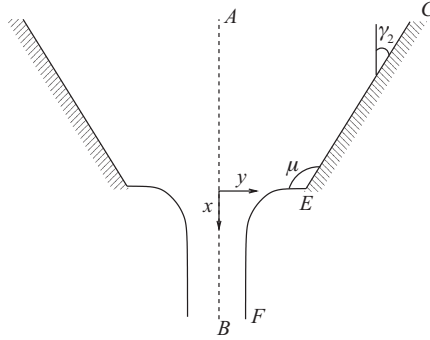


Fig. 3.40. A free surface flow emerging from a funnel. Gravity is acting vertically downwards. This flow can be obtained by rotating the flow of Figure 3.33 by 90° and reflecting it in the wall AB .

The expression (3.218) reduces to

$$w = t^{\gamma_2/\pi} \frac{[-\ln C_p(1-t)]^{1/3}}{(-\ln C_p)^{1/3}} (1+t)^{2-2\mu/\pi} \bar{G}(t), \quad (3.221)$$

where $\bar{G}(t)$ is defined by (3.219). The dynamic boundary condition (3.160) with $\beta_1 = 0$ gives

$$\frac{1}{2}(u^2 + v^2) - gx = B. \quad (3.222)$$

We define dimensionless variables by using $(Q^2/g)^{1/3}$ as the unit length and $(Qg)^{1/3}$ as the unit velocity; here Q is the value of ψ on the streamline CEF . This scaling is different from that used in Sections 3.1.1 and 3.2 since the velocity tends to infinity as $x \rightarrow \infty$ instead of approaching a constant U . In dimensionless variables (3.222) becomes

$$\frac{1}{2}(u^2 + v^2) - x = B. \quad (3.223)$$

The flow domain in the $f = (\phi + i\psi)$ -plane is, as before, the strip $0 < \psi < 1$ (see Figure 3.4). Here the point D is irrelevant since $\gamma_1 = \gamma_2$.

We will find the coefficients a_n by truncating the series in (3.221) and satisfying (3.223) at suitably chosen collocation points. Therefore we need to express x in (3.223) in terms of $w = u - iv$. This is achieved by differentiating (3.223) with respect to σ and using (3.10) and (3.38). Then the chain rule gives

$$wu_\sigma + vv_\sigma + \frac{1}{\pi} \cotan \frac{\sigma}{2} \frac{u}{u^2 + v^2} = 0. \quad (3.224)$$

The local analysis near E described at the beginning of this chapter shows that there are three possible values of μ : π , $2\pi/3$ and $\pi/2 + \gamma_2$. Numerical experimentation shows that, for a given value of $\gamma_1 = \gamma_2$, the solutions corresponding to $\mu = \pi$ and $\mu = \pi/2 + \gamma_2$ form a one-parameter family of solutions whereas there is only one solution corresponding to $\mu = 2\pi/3$. Here, and in the remaining part of the book, we use the expression to mean the computing of solutions for varying numbers of parameters. In this case, ‘numerical experimentation’ in the series representation fixing fewer, or more, parameters leads either coefficients a_n that do not decrease as n becomes very large or a divergence of the iterations.

A convenient choice for the parameter is

$$\bar{H} = \frac{1}{W}, \quad (3.225)$$

where W is the dimensionless distance between the separation point E and the wall AB . Therefore

$$\bar{H} = \frac{1}{y(\pi)}, \quad (3.226)$$

where $y(\pi)$ denotes the value of y at $\sigma = \pi$.

For $\mu = \pi$ and $\mu = \pi/2 + \gamma_2$, we truncate the infinite series within (3.221) after N terms and satisfy (3.224) at the $N - 1$ collocation points

$$\sigma_I = \frac{\pi}{2(N-1)} \left(I - \frac{1}{2} \right), \quad I = 1, 2, \dots, N-1. \quad (3.227)$$

An extra equation is obtained by satisfying (3.226), where \bar{H} is given. The value of $y(\pi)$ in (3.226) is obtained by integrating numerically the identity (3.38), where w is defined by (3.221). This gives a system of N algebraic equations for the N unknowns a_0, a_1, \dots, a_{N-1} . This system is solved by Newton’s method.

For $\beta = 2\pi/3$, there is one fewer equation since now we do not have to satisfy (3.226). Therefore again we truncate the infinite series within (3.221)

after N terms but satisfy (3.224) at the N collocation points

$$\sigma_I = \frac{1}{2N} \left(I - \frac{1}{2} \right), \quad I = 1, 2, \dots, N. \quad (3.228)$$

As before, this gives a system of N nonlinear algebraic equations that can be solved by Newton's method. We find that there are solutions for all values of $\bar{H} > 0$. Different behaviours are found for $\gamma_2 > \pi/6$ and $\gamma_2 < \pi/6$.

For $\gamma_2 < \pi/6$, there is a solution with $\mu = 2\pi/3$ for a particular value, say \bar{H}_c , of \bar{H} . Solutions with $\mu = \pi$ and $\mu = \pi/2 + \gamma_2$ occur for $\bar{H} > \bar{H}_c$ and $\bar{H} < \bar{H}_c$ respectively. Therefore

$$\mu = \pi \quad \text{when} \quad \bar{H} > \bar{H}_c, \quad (3.229)$$

$$\mu = \frac{2\pi}{3} \quad \text{when} \quad \bar{H} = \bar{H}_c, \quad (3.230)$$

$$\mu = \frac{\pi}{2} + \frac{\gamma_2}{2} \quad \text{when} \quad \bar{H} < \bar{H}_c. \quad (3.231)$$

The solutions corresponding to (3.229) and (3.231) approach the solution corresponding to (3.230) as \bar{H} approaches \bar{H}_c from above and from below respectively. The value of \bar{H}_c depends on the value of γ_2 .

For $\gamma_2 > \pi/6$, all solutions with $\bar{H} > 0$ are characterised by $\mu = \pi$. This is consistent with the fact that the local analysis (see Figure 3.38) shows that there are no solutions with $\mu = 2\pi/3$ or $\mu = \pi/2 + \gamma_2$ when $\gamma_2 > \pi/6$.

These results are illustrated in Figure 3.41, where we plot values of the velocity q_E at the separation point E versus \bar{H} for various values of γ_2 .

The solutions with $\mu = 2\pi/3$ and $\mu = \pi/2 + \gamma_2$ have stagnation point at E and are therefore characterised by $q_E = 0$. For $\gamma_2 \geq \pi/6$, $q_E \neq 0$ for all $\bar{H} > 0$ and $q_E \rightarrow 0$ as $\bar{H} \rightarrow 0$. For $\gamma_2 < \pi/6$, $q_E \rightarrow 0$ as $\bar{H} \rightarrow \bar{H}_c$ and $q_E = 0$ for $\bar{H} < \bar{H}_c$. Therefore the curves corresponding to $\gamma_2 = \pi/4$ and $\gamma_2 = \pi/6$ approach 0 as $\bar{H} \rightarrow 0$, whereas the curve corresponding to $\gamma_2 = \pi/12$ intersects the horizontal axis at the value $\bar{H} = \bar{H}_c \approx 0.528$.

Typical free surface profiles are shown in Figures 3.42–3.45.

The three profiles of Figures 3.42–3.44 are for $\gamma_2 = \pi/12$. Figure 3.42 corresponds to $\bar{H} = 0.81$, i.e. the case (3.229). The free surface leaves the wall tangentially. Both the free surface and the wall position can be seen in the figure (the separation point E corresponds to the point on the curve with ordinate $y = 0$). Figure 3.43 shows the profile for $\bar{H} = \bar{H}_c \approx 0.528$ (case (3.230)). There is a $2\pi/3$ angle between the free surface and the wall at the separation point. Figure 3.44 is the solution for $\bar{H} = 0.25$. Since

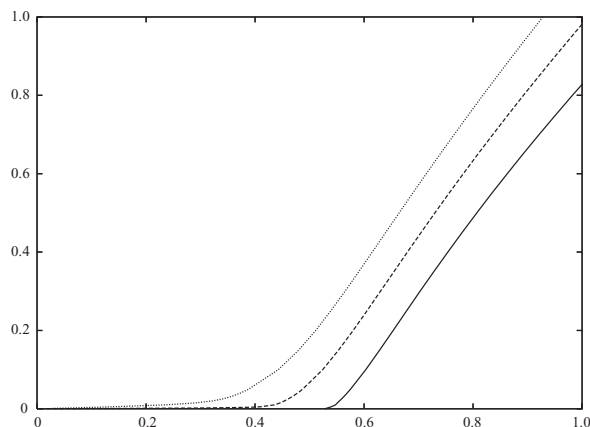


Fig. 3.41. Values of the dimensionless velocity q_E at the separation point E versus \bar{H} (see (3.225)). The values of γ_2 corresponding to the curves from left to right are $\pi/4$, $\pi/6$ and $\pi/12$.

$\bar{H} < \bar{H}_c$, it corresponds to the case (3.231). The free surface is horizontal at the separation point.

The profile in Figure 3.45 corresponds to $\gamma_2 = \pi/6$ and $q_E = 0.5$. The free surface leaves the wall tangentially. This profile is typical in the sense that all the solutions with $\gamma_2 = \pi/6$ leave the wall tangentially (see Figure 3.41).

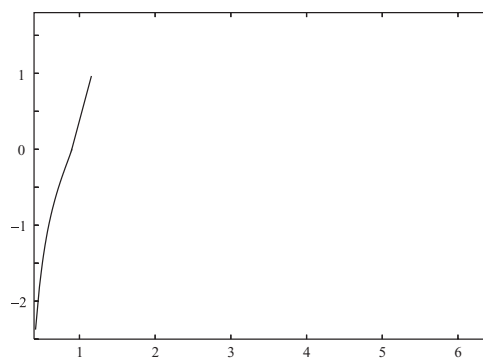


Fig. 3.42. A free surface profile EF of Figure 3.40 for $\gamma_2 = \pi/12$. The ordinate of the separation point is zero. The dimensionless velocity q_E at the separation point is 0.5. The free surface leaves the wall tangentially and $\mu = \pi$.

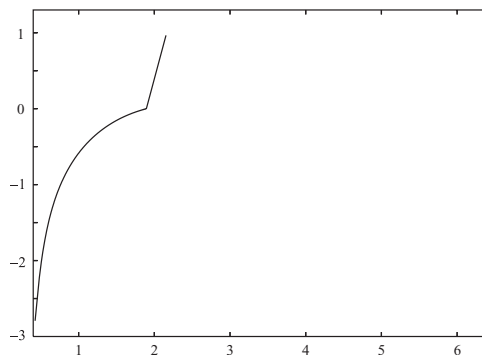


Fig. 3.43. A free surface profile EF of Figure 3.40 for $\gamma_2 = \pi/12$. The ordinate of the separation point is zero. This profile corresponds to $\mu = 2\pi/3$ and $\bar{H} = \bar{H}_c \approx 0.528$.

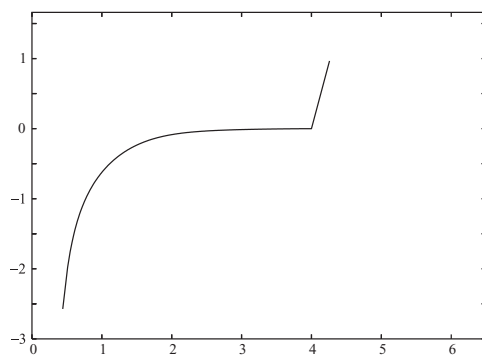


Fig. 3.44. A free surface profile EF of Figure 3.40 for $\gamma_2 = \pi/12$ and $\bar{H} = 0.25$. The ordinate of the separation point is zero. The free surface is horizontal at the separation point.

3.3.2 Solutions with $\beta_1 = 0$ (nozzles and bubbles)

Next we present computations for $\gamma_1 = \gamma_2 = 0$ (see Figure 3.46). This configuration differs from that of Figure 3.40 because the flow approaches a uniform stream with constant velocity U as $x \rightarrow -\infty$ instead of approaching a zero velocity. This problem was considered by many investigators (see [18], [62], [63], [165], [166], [169] and others). The study presented below follows Vanden-Broeck [165], [166] and [169].

We will describe the problem by reverting to dimensionless variables in which the unit length is $H = Q/U$ and the unit velocity is U . Then the

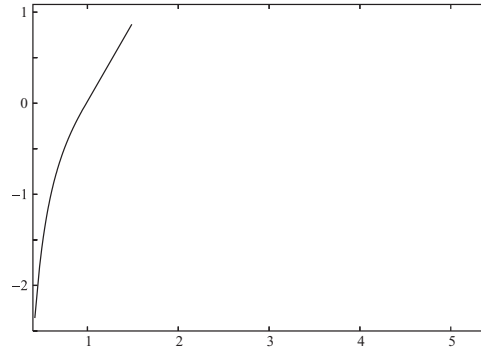


Fig. 3.45. A free surface profile EF of Figure 3.40 for $\gamma_2 = \pi/6$. The ordinate of the separation point is zero. The dimensionless velocity q_E at the separation point is 0.5. The free surface leaves the wall tangentially.

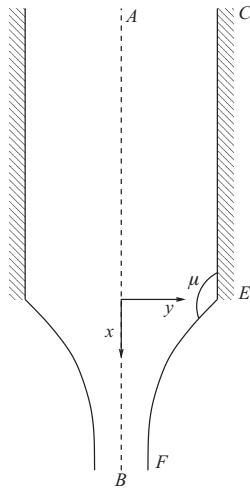


Fig. 3.46. The free surface flow from a nozzle.

dynamic boundary condition (3.160) becomes, in dimensionless variables,

$$u^2 + v^2 - \frac{1}{F^2}x = B, \tag{3.232}$$

where F is the Froude number defined by

$$F = \frac{U}{(2gH)^{1/2}}. \tag{3.233}$$

We note that F is related to \bar{H} in (3.225) by

$$F = \left(\frac{\bar{H}^3}{2} \right)^{1/2}. \quad (3.234)$$

The factor $2^{1/2}$ in (3.233) was introduced for consistency with previous calculations. Similarly (3.224) becomes

$$2uu_\sigma + 2vv_\sigma + \frac{1}{\pi F^2} \cotan \frac{\sigma}{2} \frac{u}{u^2 + v^2} = 0. \quad (3.235)$$

The flow of Figure 3.46 has interesting applications. First, it clearly models a jet emerging from a nozzle. Second, it models a bubble rising in a tube when viewed in a frame of reference moving with the bubble (see Figure 3.47). This follows from the symmetry of the flow: the portion EF of the bubble surface in Figure 3.47 is identical, for the same value of the Froude number F , to the portion EF of the jet surface in Figure 3.46.

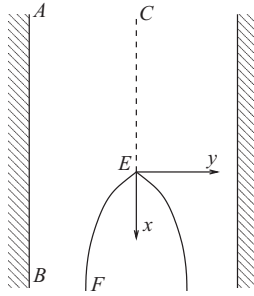


Fig. 3.47. A ‘bubble’ rising in a tube, viewed in a frame of reference moving with the bubble. Physical bubbles are characterised by a continuous slope at the apex.

Returning to our calculation, we represent the complex velocity w by the expansion

$$w = \frac{[-\ln C(1-t)]^{1/3}}{(-\ln C)^{1/3}} (1+t)^{2-2\mu/\pi} \bar{G}(t). \quad (3.236)$$

We shall now do new calculations, representing $\bar{G}(t)$ by (3.220) instead of (3.219). Therefore we write

$$\bar{G}(t) = \exp \left(\sum_{n=1}^{\infty} a_n t^n \right), \quad (3.237)$$

where we have set $a_0 = 0$ so that $w = 1$ at $t = 0$.

As for the previous solutions with $\gamma_1 = \gamma_2 \neq 0$, there are solutions with $\mu = \pi$, $\mu = 2\pi/3$ and $\mu = \pi/2 + \gamma_2 = \pi/2$. The solution for $\mu = 2\pi/3$ corresponds to a critical value $F_c \approx 0.3578$ of the Froude number F . Solutions with $\mu = \pi$ occur for $F > F_c$, and those with $\mu = \pi/2 + \gamma_2 = \pi/2$ occur for $F < F_c$. Therefore we have

$$\mu = \pi \quad \text{when} \quad F > F_c, \quad (3.238)$$

$$\mu = \frac{2\pi}{3} \quad \text{when} \quad F = F_c, \quad (3.239)$$

$$\mu = \frac{\pi}{2} \quad \text{when} \quad F < F_c. \quad (3.240)$$

As expected these solutions are the limit of those of Figure 3.40 as $\gamma_2 \rightarrow 0$. In particular, the three values (3.229)–(3.231) reduce to (3.238)–(3.240) as $\gamma_2 \rightarrow 0$, with

$$H_c = (2F_c^2)^{1/3}. \quad (3.241)$$

For the solutions with $\mu = \pi$ and $\mu = \pi/2$, we truncate the series (3.237) after N terms and satisfy (3.235) at the N collocation points (3.228). For a given value of F , this gives a system of N algebraic equations with N unknowns. This system is solved by Newton's method. For $\mu = 2\pi/3$, F is one unknown. Therefore we truncate the series (3.237) after $N - 1$ terms and satisfy (3.235) at the N collocation points (3.228). This leads again to a system of N algebraic equations with N unknowns.

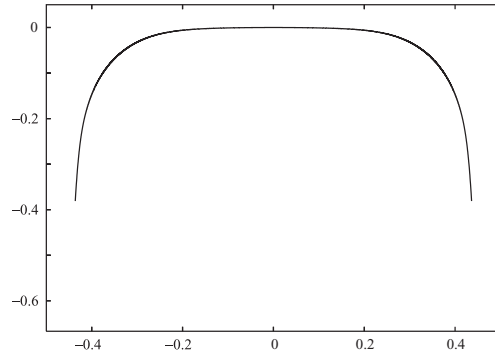
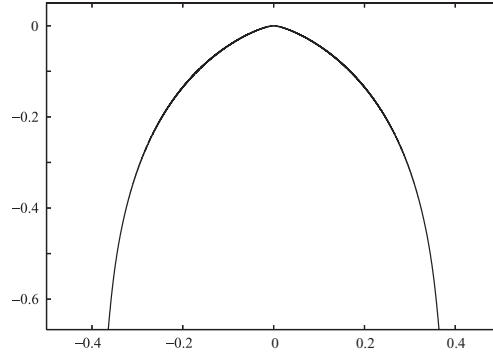
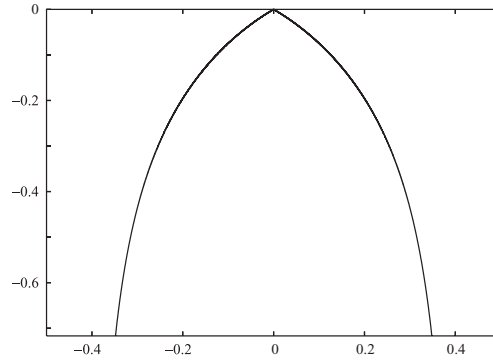


Fig. 3.48. Rising bubble in a tube for $F = 0.1$.

The solutions we have computed model the flow emerging from a nozzle (see Figure 3.46) or a bubble rising in a tube (see Figures 3.47–3.52). On physical grounds we expect a bubble to be characterised by a continuous

Fig. 3.49. Rising bubble in a tube for $F = 0.3$.Fig. 3.50. Rising bubble in a tube for $F = F_c$. There is a 120° angle at the apex of the bubble.

slope at its apex. This implies that $\mu = \pi$. Therefore all the solutions for $0 < F < F_c$ should model a rising bubble. However, experiments (see [32] and [107]) showed that bubbles are only observed for a unique value,

$$F_e \approx 0.25, \quad (3.242)$$

of the Froude number. Clearly the value F_e is in the interval $0 < F < F_c$ for which we have computed bubbles but the question is to find what is special about the value F_e . This is an example of a ‘selection problem’. We have already encountered such a problem in Section 3.2.2. There we found that cavitating flow past a circular cylinder could be calculated for all values $\gamma^* < \bar{\gamma} < \gamma^{**}$ when surface tension was neglected. We then showed that a unique solution, for $\bar{\gamma} \approx 55^\circ$, could be selected by solving the problem with $T \neq 0$ and then taking the limit as $T \rightarrow 0$. We shall show in Section 3.4

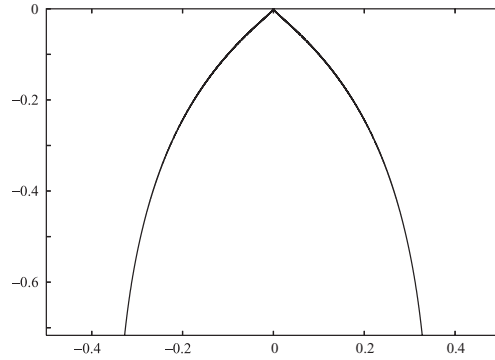


Fig. 3.51. Rising bubble in a tube for $F = 0.4$. A cusp has appeared at the apex.

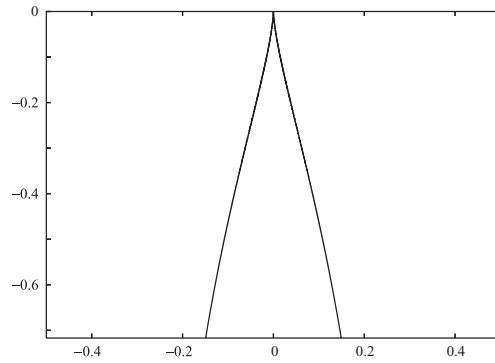


Fig. 3.52. Rising bubble in a tube for $F = 1$. There is a cusp at the apex of the free surface profile.

that a unique bubble can again be selected by introducing surface tension and then taking the limit as $T \rightarrow 0$.

We conclude this section by mentioning that our findings with $T = 0$ are consistent with analytical results derived by Garabedian [62]. Garabedian [62] proved that there are mathematical solutions describing ‘bubbles’ with a continuous slope at the apex for all values of F smaller than a critical value F_c . He then used an energy argument to suggest that the only physically significant solution is the one for which $F = F_c$. In addition he showed that $F_c > 0.2363$. However, our computations using series truncation showed that $F_c \approx 0.36$. This value is about 40 percent higher than the experimental value (3.242). Furthermore the solution corresponding to $F = F_c$ does not have

a continuous slope at the apex since $\mu = 2\pi/3$ (see Figure 3.50). Therefore Garabedian's energy argument does not select the relevant solution.

3.3.3 Solutions with $\beta_1 = \pi/2$ (flow under a gate with gravity)

In this section we consider solutions for the flow configuration of Figure 3.37 with $\beta_1 = \pi/2$. The analysis follows [171] and [94]. We introduce dimensionless variables by using U as the unit velocity and H as the unit length. The Bernoulli equation (3.160) can be written as

$$\frac{1}{2}(u^2 + v^2) + \frac{1}{F^2}y = B, \quad (3.243)$$

where

$$F = \frac{U}{(gH)^{1/2}}. \quad (3.244)$$

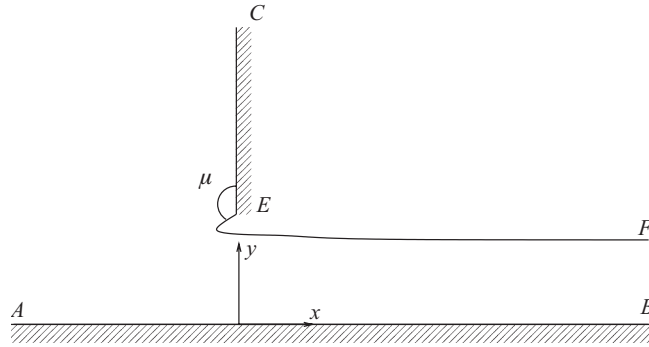


Fig. 3.53. The flow under a gate showing, the angle μ between the free surface EF and the wall CE .

We represent the complex velocity w by

$$w = \left(\frac{t-d}{1-td} \right)^{(\gamma_2-\gamma_1)/\pi} t^{\gamma_1/\pi} \frac{(t+1)^{2-2\mu/\pi}}{2} e^{A(1-t)^{2\mu}} G(t), \quad (3.245)$$

where A is a real constant to be found as part of the solution. The function $G(t)$ is free of singularities. The condition $w = 1$ at $t = 1$ implies that $G(1) = 0$. Therefore we can write

$$G(t) = e^{\sum_{n=1}^{\infty} a_n (t^n - 1)}. \quad (3.246)$$

Following the derivation leading to (3.224) we rewrite (3.243) as

$$uu_\sigma + vv_\sigma - \frac{1}{\pi F^2} \cotan \frac{\sigma}{2} \frac{v}{u^2 + v^2} = 0. \quad (3.247)$$

We now present explicit computations for $\gamma_1 = \gamma_2 = \pi/2$ (i.e. for the flow configuration of Figure 3.53). As we shall see, these numerical computations show that there are solutions corresponding to the three possible values π , $\pi/2$ and $2\pi/3$ of μ .

We first calculate the solutions corresponding to $\mu = \pi$ (i.e. solutions for which the free surface leaves the wall tangentially). We truncate the infinite series in (3.245) after $N - 2$ terms and introduce the $N - 1$ collocation points

$$\sigma_I = \frac{\pi}{N-1} \left(I - \frac{1}{2} \right), \quad I = 1, 2, \dots, N-1. \quad (3.248)$$

We then use (3.245) to evaluate $u - iv$ at the mesh points (3.248) and obtain $N - 1$ algebraic equations by satisfying (3.247) at these points. One more equation is given by (3.216). The final equation is obtained by fixing a parameter characterising the flow. An obvious choice for this parameter is the Froude number F . However, the computations reveal that there can be several solutions corresponding to the same value of the Froude number; a better choice for the parameter is the dimensionless velocity at the separation point E . Therefore we set

$$q_E = |(w)_{t=-1}|. \quad (3.249)$$

This leads to a system of $N + 1$ equations for the $N + 1$ unknowns $a_1, a_2, \dots, a_{N-2}, A, F$ and $\bar{\mu}$.

Typical profiles are presented in Figures 3.54 and 3.55.

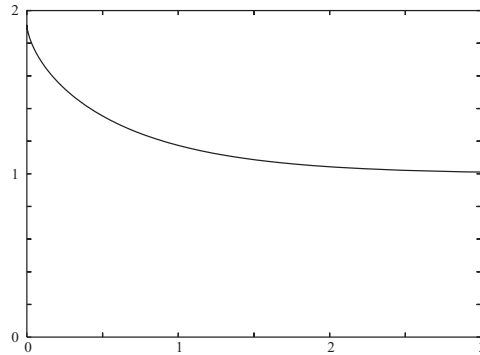


Fig. 3.54. Computed free surface profile for the flow under a gate with $F = 2$. The angle μ is equal to π .

The values of the dimensionless velocity q_E at the separation point E versus the Froude number F are shown in Figure 3.56.

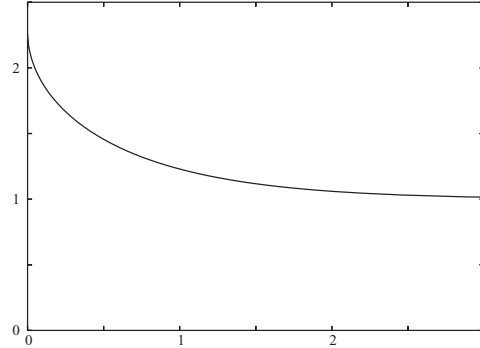


Fig. 3.55. Computed free surface profile for the flow under a gate with $F = 1.8$. The angle μ is equal to π .

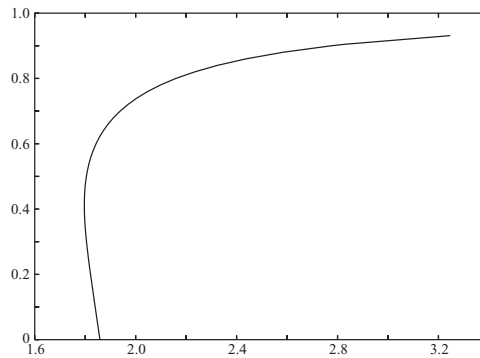


Fig. 3.56. Values of the dimensionless velocity q_E at the separation E versus the Froude number F .

As $F \rightarrow \infty$, so $q_E \rightarrow 1$ and the solution reduces to the free streamline solution (3.39). As q_E decreases from 1, the Froude number F first decreases to a minimum value $F_2 \approx 1.8$ and then increases up to the value $F_1 \approx 1.87$. The value $F = F_1$ corresponds to $q_E = 0$. These results show that a unique solution with $\mu = \pi$ exists for all values of $F > F_1$. For $F_2 < F < F_1$, two different solutions with $\mu = \pi$ are possible. For $F < F_2$, there are no solutions with $\mu = \pi$. The coefficients a_n were found to decrease rapidly as n increases. However, as q_E approaches zero, the rate of convergence of the series deteriorates and larger and larger values of N are needed to obtain accurate solutions. This is due to the fact that solutions with $q_E = 0$ must correspond to $\mu = \pi/2$ or $\mu = 2\pi/3$. Therefore they cannot be computed by the expansion (3.245), (3.246) with $\mu = 0$.

We now consider solutions with $\mu = 2\pi/3$. Numerical experimentation shows that there is only one solution. This is the limit of the family of solutions with $\mu = \pi$ as $q_E \rightarrow 0$. To calculate it, we set $\mu = 2\pi/3$ in (3.245), truncate the infinite series in (3.246) after $N - 3$ terms and satisfy (3.247) at the mesh points (3.248). This leads to $N - 1$ equations for the N unknowns $a_1, a_2, \dots, a_{N-3}, A, F$ and $\bar{\mu}$. The last equation is (3.216). The resulting numerical solution is shown in Figure 3.57.

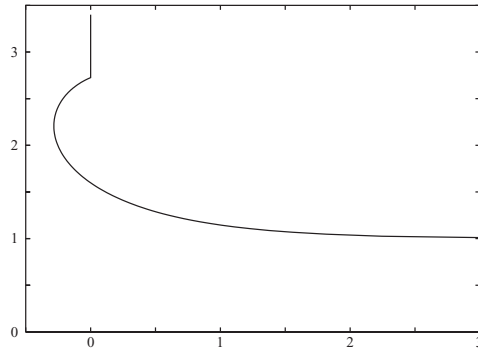


Fig. 3.57. Computed free surface profile for the flow under a gate with $\mu = 2\pi/3$. The solution is unique and the corresponding value of the Froude number is $F = F_1 \approx 1.86$.

Finally, we look for solutions with $\mu = \pi/2$. Numerical experimentation shows that there is a one-parameter family of solutions (the parameter can be chosen as the Froude number F). This family exists for $F > F_1$. As $F \rightarrow F_1$, the solutions approach the solution corresponding to $F = F_2$ and $q_E = 0$. A typical free surface profile is shown in Figure 3.58. To compute these solutions we set $\mu = \pi/2$ in (3.245), truncate the infinite series in (3.246) after $N - 2$ terms and again satisfy (3.247) at the mesh points (3.248). For a given value of F , this leads to $N - 1$ equations for the N unknowns $a_1, a_2, \dots, a_{N-2}, A$ and $\bar{\mu}$. The last equation is given as before by (3.216).

Although these solutions are mathematically interesting they are unstable since in them the heavy fluid is lying on top of the light one.

Values of the contraction ratio C_c versus F for the solution branch with $\mu = \pi$ are shown in Figure 3.59.

Budden and Norbury [24] derived the following asymptotic solution for C_c :

$$C_c = \frac{\pi}{\pi + 2} - \frac{(4j + 2)\pi^2 + \pi^3}{(\pi + 2)^5} \alpha - 0.0007\alpha^2 + \dots \quad (3.250)$$

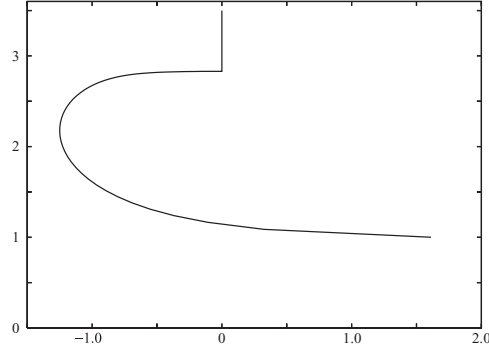


Fig. 3.58. Computed free surface profile for the flow under a gate with $\mu = \pi/2$. The value of the Froude number is $F \approx 1.9$.

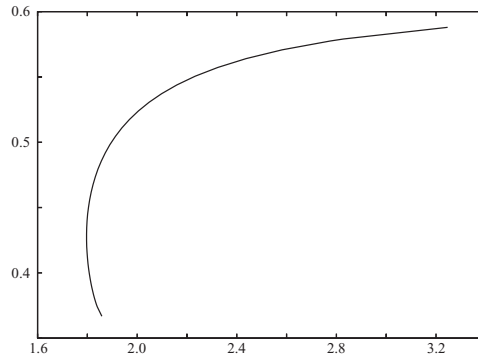


Fig. 3.59. Values of the contraction ratio C_c versus the Froude number F .

Here $j = 0.9150965\dots$ and α is defined by

$$\alpha = \frac{F^4}{4} \left(1 - \delta^2 + \frac{2}{F^2} \right)^3. \quad (3.251)$$

For $F = 2$, the value of the contraction ratio predicted by (3.250) agrees with the numerical results within one per cent.

3.4 The combined effects of gravity and surface tension

When gravity is included in the dynamic boundary condition and surface tension is neglected, only three values of the angle μ between the free surface EF and the rigid wall DE are allowed for the flow configuration of Figure 3.37 ($\mu = \pi$, $\mu = 2\pi/3$ and $\mu = \pi/2 + \gamma_2$). When surface tension is included

and gravity neglected, all values of μ are in principle possible. Therefore we can expect interesting behaviours to occur when both gravity and surface tension are taken into account, especially in the limit $T \rightarrow 0$.

3.4.1 Rising bubbles in a tube

We present our main findings for the flow of Figure 3.46. The analysis follows Vanden-Broeck [166]. We recall that this configuration also models the flow past a bubble in a tube (see Figure 3.47). As in Section 3.3.2 we assume without loss of generality that there is an angle μ between the wall CE and the free surface EF at the point E (see Figure 3.46). If the free surface leaves the wall tangentially then $\mu = \pi$. If $\mu < \pi$ then the flow near E is locally a flow inside an angle and the speed at E is zero. If $\mu > \pi$ then the flow near E is locally a flow around a corner and the speed at E is infinite. Following the analysis in Section 3.3.2, we introduce dimensionless variables by taking the constant velocity U at $x = \infty$ as the reference velocity and the distance H between AB and CE as the reference length. The dynamic boundary condition on the free surface EF can be written in dimensionless variables as

$$\frac{1}{2}q^2 - \frac{1}{F^2}x + \frac{2}{\alpha}K = B. \quad (3.252)$$

Here q is the magnitude of the velocity variable, K the curvature of the free surface EF , B the Bernoulli constant, F the Froude number defined in (3.233) and α the Weber number, defined by

$$\alpha = \frac{2\rho U^2 H}{T}. \quad (3.253)$$

As noted in Section 3.3.2 only values of $\mu \leq \pi$ are allowed when $T = 0$ because the dynamic boundary condition (3.160) requires the velocity q_E at the point E in Figure 3.46 to be finite. However, when $T \neq 0$, values of $\mu > \pi$ are in principle possible because an infinite value of q in (3.252) can be balanced by an infinite value of the curvature. Examples of such flows with surface tension included and gravity neglected were covered in Section 3.2. In this section we show examples of gravity–capillary flows for which q_E is infinite. The physical relevance of such flows can of course be questioned. However, we shall see that their consideration is crucial in constructing systematically other physical solutions.

The flow configuration in the complex potential plane is shown in Figure 3.4. We map it into the complex t -plane by using (3.8). The complex t -plane is illustrated in Figure 3.5. Proceeding as in Section 3.3.1, we write

the complex velocity w as

$$w = \frac{[-\ln C_p(1-t)]^{1/3}}{(-\ln C_p)^{1/3}}(1+t)^{2-2\mu/\pi}G(t), \quad (3.254)$$

where

$$G(t) = e^{\sum_{n=1}^{\infty} a_n t^n}. \quad (3.255)$$

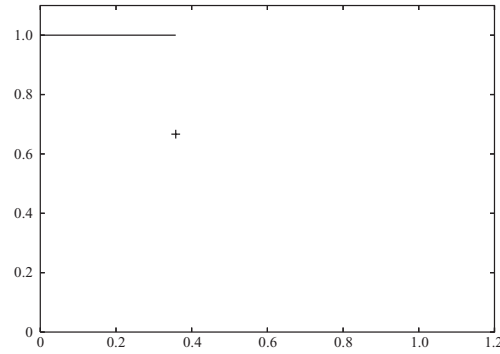


Fig. 3.60. Values of ν versus F for the flow configuration of Figure 3.47 when $\alpha = \infty$, i.e. $T = 0$.

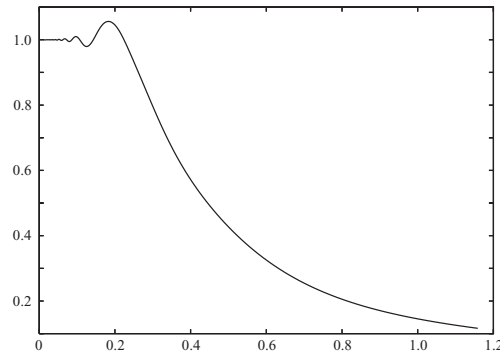


Fig. 3.61. Values of ν versus F for the flow configuration of Figure 3.47 when $\alpha = 10$.

Next we differentiate (3.252) with respect to ϕ and use (3.10) and the chain rule to obtain

$$2uu_\sigma + 2vv_\sigma + \frac{1}{\pi F^2} \cotan \frac{\sigma}{2} \frac{u}{u^2 + v^2} + \frac{4\pi}{\alpha} \frac{\partial}{\partial \sigma} \left[\tan \frac{\sigma}{2} \frac{uv_\sigma - vu_\sigma}{(u^2 + v^2)^{1/2}} \right] = 0. \quad (3.256)$$

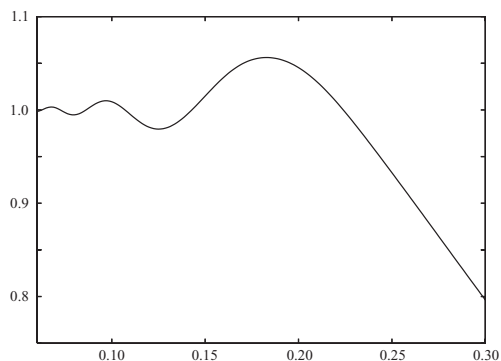


Fig. 3.62. Enlargement of part of Figure 3.61 showing clearly oscillations around 1.0.

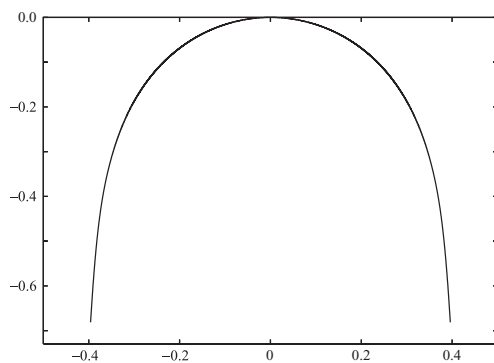


Fig. 3.63. The selected bubble for $T = 0$. The value of the Froude number is $F = F^* \approx 0.23$.

We truncate the infinite series in (3.255) after $N-1$ terms and satisfy (3.256) at the mesh points

$$\sigma_I = \frac{1}{2N} \left(I - \frac{1}{2} \right), \quad I = 1, \dots, N. \quad (3.257)$$

This is achieved by substituting (3.254) and its derivative with respect to σ into (3.256). It leads to N nonlinear equations for the N unknowns a_1, \dots, a_{N-1} and μ . This system is solved by Newton's method for given values of F and α .

We start the presentation of the numerical results by recalling the findings of Section 3.3.2 when $T = 0$ (i.e. $\alpha = \infty$). They are shown graphically in

Figure 3.60 where we plot the parameter

$$\nu = 2 \frac{\pi - \mu}{\pi} \quad (3.258)$$

versus F . There is a unique solution with $\mu = 2\pi/3$ (i.e. $\nu = 2/3$) for $F = F_c \approx 0.36$. Solutions with $\mu = \pi/2$ (i.e. $\nu = 1$) and $\mu = \pi$ (i.e. $\nu = 0$) occur for $F < F_c$ and $F > F_c$ respectively. The curve of Figure 3.60 is discontinuous with a jump at $F = F_c$. When surface tension is included in the dynamic boundary condition, the discontinuity disappears and the curve of Figure 3.60 is replaced by a continuous one. This is illustrated in Figure 3.61, where we present values of ν versus F for $\alpha = 10$. An interesting feature is that the curve of Figure 3.61 oscillates infinitely often around $\nu = 1$. An enlargement of Figure 3.61 is shown in Figure 3.62. As F decreases, the amplitude and wavelength of the oscillations decrease. These results suggest that there is a countably infinite set of values of F for which $\nu = 1$. We denote this set by

$$F_i^*, \quad i = 1, 2, \dots, \quad (3.259)$$

where

$$F_1^* > F_2^* > F_3^* > \dots$$

We recall that physically relevant bubbles are identified as those for which $\nu = 1$. Therefore all bubbles with $F < F_c$ are physically relevant when $T = 0$ whereas only those corresponding to the set (3.259) are physically relevant when $T \neq 0$.

The numerical computations show that, for each given value of i ,

$$F_i^* \rightarrow F^* \quad \text{as} \quad \alpha \rightarrow \infty, \quad (3.260)$$

where

$$F^* \approx 0.23. \quad (3.261)$$

This is shown in Figure 3.64, where we plot values of F_1 versus α^{-1} . As $T \rightarrow 0$ (i.e. $\alpha^{-1} \rightarrow 0$), $F_1 \rightarrow F^*$ in agreement with (3.260).

Our findings can be summarised as follows. When $T = 0$, there is a bubble (with $\mu = \pi$) for each value of $0 < F < F_c$. When $T \neq 0$, there is a bubble (with $\mu = \pi$) for a discrete set of values of F (see (3.259)). As $T \rightarrow 0$, the discrete set reduces to a unique value $F = F^*$ of F . Therefore we have succeeded in selecting a unique solution by including surface tension and taking the limit as $T \rightarrow 0$. Moreover the selected value $F^* \approx 0.23$ is close to the experimental value $F_c \approx 0.25$ (see [32] and [107]).

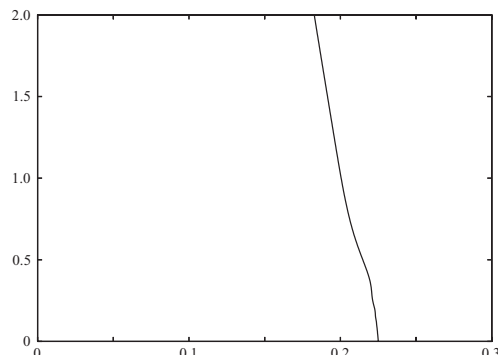


Fig. 3.64. Values of α^{-1} versus F_1^* . As $\alpha^{-1} \rightarrow 0$, $F_1 \rightarrow F_1^* \approx 0.23$.

3.4.2 Fingering in a Hele Shaw cell

Another classical example of the selection of solutions via surface tension occurs in the study of fingering in a Hele Shaw cell. This problem can be motivated as follows. It is well known that an instability may occur in a porous medium when a less viscous fluid drives a more viscous fluid (Saffman and Taylor [132]). To study this instability, experiments have been performed in a Hele Shaw cell, a channel formed by two closely spaced parallel glass plates; this provides a model of a two-dimensional flow through a porous medium. It was found that the unstable interface develops a number of ‘fingers’. After some time, one finger dominates and suppresses the growth of the others and the flow reaches a steady state in which a single finger propagates without change of shape. McLean and Saffman [109] modelled this finger by a two-dimensional potential flow with surface tension included at the interface (see Figure 3.65). They denoted by U the velocity of the finger, $2a$ the lateral width of the channel, b the transverse thickness, T the surface tension and $\tilde{\mu}$ the viscosity (here we use a tilde to avoid confusion with the angle μ used earlier in this section). In addition they denoted the ratio of the width of the finger and the width of the channel by λ .

Taking a as the unit length and $(1 - \lambda)U$ as the unit velocity, McLean and Saffman derived a nonlinear integro-differential equation for the unknown shape S of the free surface:

$$\ln q(S) = -\frac{S}{\pi} \int_0^1 \frac{\theta(S')}{S'(S' - S)} dS', \quad (3.262)$$

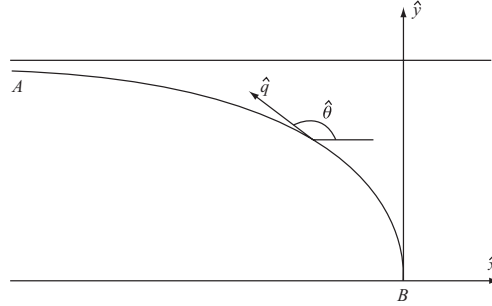


Fig. 3.65. Model for a finger in a Hele Shaw cell. Only half the finger is shown.

$$\kappa q S \frac{d}{dS} \left(q S \frac{d\theta}{dS} \right) - q = -\cos \theta, \quad (3.263)$$

$$\theta(0) = 0, \quad q(0) = 1, \quad (3.264)$$

$$\theta(1) = -\frac{\pi}{2}, \quad q(1) = 0. \quad (3.265)$$

Here

$$\theta = \hat{\theta} - \pi, \quad (3.266)$$

$$q = (1 - \lambda)\hat{q}, \quad (3.267)$$

$$\kappa = \frac{Tb^2\pi^2}{12\mu U a^2(1 - \lambda)^2}. \quad (3.268)$$

The integral in (3.262) is of Cauchy principal-value form. The variables $\hat{\theta}$ and \hat{q} in (3.266) and (3.267) are defined in terms of the dimensionless complex velocity $\hat{u} - i\hat{v}$ by the relation

$$\hat{u} - i\hat{v} = \hat{q}e^{-i\hat{\theta}}. \quad (3.269)$$

The flow configuration is illustrated in Figure 3.65. The \hat{x} -axis is parallel to the walls of the channel and is the axis of symmetry of the finger. The points A and B correspond to $S = 0$ and $S = 1$ respectively.

After a solution for θ and q is obtained, the shape of the finger is given by

$$\hat{x}(S) + i\hat{y}(S) = -\frac{1 - \lambda}{\pi} \int_0^1 \frac{e^{i\theta}}{Sq} dS. \quad (3.270)$$

For $\kappa = 0$ (i.e. in the absence of surface tension), Saffman and Taylor [132] obtained the following exact solution:

$$q = \left[\frac{(1-S)/(1-\lambda)^2}{(1-\lambda)^2 + S(2\lambda-1)} \right]^{1/2}, \quad (3.271)$$

$$\theta = \cos^{-1}q. \quad (3.272)$$

The solution (3.271), (3.272) leaves the parameter λ undetermined. In other words a solution can be found for each value of $0 < \lambda < 1$. This finding is not consistent with experiments, which show that for small values of the surface tension there is only one finger, corresponding to $\lambda \approx 0.5$. This is again a selection problem and can be resolved by solving the problem with surface tension and then taking the limit as the surface tension approaches zero.

Early numerical calculations with $\kappa \neq 0$ were performed by McLean and Saffman [109], who identified one family of solutions. Romero [129] then found two other families. As we shall see there is in fact a countably infinite set of families of solutions.

There is a strong analogy between the fingering problem and the bubble problem of Figure 3.47. The procedure to find the discrete set (3.259) allowed the angle μ to be found as part of the solution. Therefore we shall use a similar approach for the fingering problem. The analysis follows Vandenberg [161].

We define a modified problem that has solutions for all values of λ and κ . This modified problem is obtained by replacing (3.265) simply by

$$q(1) = 0. \quad (3.273)$$

Therefore $\theta(1)$ becomes an unknown to be found as part of the solution.

We solve the modified problem defined by (3.262)–(3.264) and (3.273) and obtain solutions for all values of λ and κ . We will then obtain solutions of the original problem by selecting among the solutions of the modified problem those for which $\theta_1 = -\pi/2$.

Following McLean and Saffman [109] we introduce the change of variables

$$S^\tau = 1 - \zeta^\gamma. \quad (3.274)$$

Here τ is the smallest root of

$$\frac{1}{\tau^2} \cotan \pi\tau = \kappa. \quad (3.275)$$

With (3.274), θ is twice differentiable with respect to ζ at both end points. McLean and Saffman [109] chose $\gamma = 2$ in (3.274). In order to solve the modified problem we will choose $\gamma = 4$.

We introduce the N mesh points

$$\zeta_I = \frac{I-1}{N}, \quad I = 1, \dots, N. \quad (3.276)$$

We also define the unknowns

$$\theta_I = \theta(1 - \zeta_I^\gamma), \quad I = 1, \dots, N. \quad (3.277)$$

We discretise the system (3.262)–(3.264) and (3.273) by following the procedure outlined by McLean and Saffman [109]. Thus we obtain $N - 1$ nonlinear algebraic equations for the $N - 1$ unknowns $\theta_I, I = 2, \dots, N$. For given values of λ and κ this system is solved by Newton's method.

In Figure 3.66 we present numerical values of $\theta(1)$ versus λ for $\kappa = 0.273$. As λ approaches zero, $\theta(1) \rightarrow -\pi$ and the finger collapses on the negative \tilde{x} -axis. As λ approaches unity, $\theta(1)$ oscillates infinitely often around $-\pi/2$. An enlargement of part of Figure 3.66 is shown in Figure 3.67 to illustrate the oscillations clearly.

Figures 3.66 and 3.67 show that there is a countably infinite set of values of λ for which $\theta(1) = -\pi/2$. We denote this set by

$$\lambda_i, \quad i = 1, 2, 3, \dots \quad (3.278)$$

where

$$\lambda_1 > \lambda_2 > \lambda_3 \cdots$$

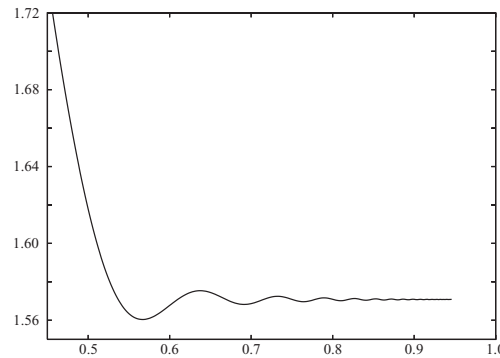


Fig. 3.66. Values of $\theta(1)$ versus λ for $\kappa = 0.273$.

The solutions corresponding to the values (3.278) of λ are the solutions of the original problem.

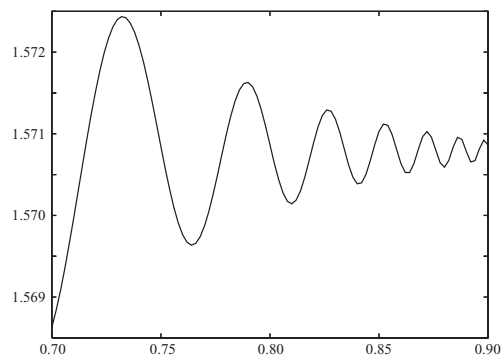


Fig. 3.67. Enlargement of part of Figure 3.66 showing clearly the oscillations around $\pi/2$.

Vanden-Broeck [161] showed numerically that, for a given value of i ,

$$\lambda_i \rightarrow \frac{1}{2} \quad \text{as } \kappa \rightarrow 0. \quad (3.279)$$

It can be seen from relation (3.279) that a unique solution corresponding to $\lambda = 1/2$ is selected in the limit as the surface tension tends to zero. We note that (3.279) is comparable with (3.260). This finding is illustrated in Figure 3.68, where values of λ_1 , λ_2 and λ_3 versus κ are plotted. As $\kappa \rightarrow 0$, the three curves approach $\lambda = 1/2$.

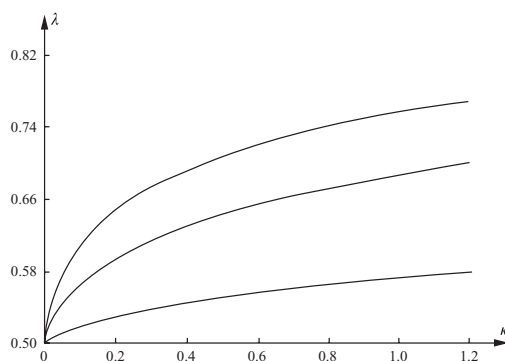


Fig. 3.68. Values of λ versus κ .

3.4.3 Further examples involving rising bubbles

We now return to potential flows and present three other examples of free surface flows for which a unique solution can be selected by taking the limit $T \rightarrow 0$. These flows are similar to the flow past a bubble shown in Figure 3.47. The first two are given in Figures 3.69 and 3.70. They model a two-dimensional bubble rising at a constant velocity U in an unbounded fluid when viewed in a frame of reference moving with the bubble. Both configurations include a model for the wake behind the bubble. In that sense they are improvements on the flow of Figure 2.2, in which the wake was neglected. The free surface flows of Figures 3.69 and 3.70 can be solved by series truncation methods similar to those used earlier in this section. Details can be found in [170] and [174] respectively. We summarise here the main results.

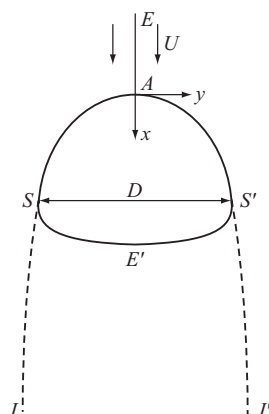


Fig. 3.69. A free streamline model for a rising bubble.

In Figure 3.69, a free streamline model (similar to the cavitating models of Section 3.1.2) is used. This implies that the velocity is equal to U on the boundaries SJ and $S'J'$ of the wake. When surface tension is neglected there is one solution for each value of the Froude number

$$F = \frac{U}{(gD)^{1/2}}, \quad (3.280)$$

where D is defined in Figure 3.69. If we denote by μ the angle between the

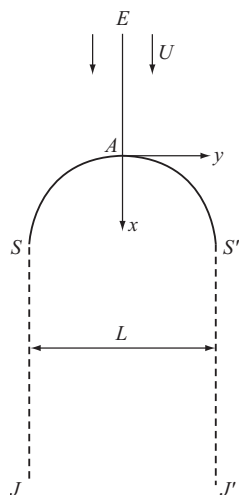


Fig. 3.70. Joukovskii's model for a rising bubble.

symmetry line EA and the free surface AS then it is found that

$$\mu = \frac{\pi}{2} \quad \text{when } F < F_c, \quad (3.281)$$

$$\mu = \frac{2\pi}{3} \quad \text{when } F = F_c, \quad (3.282)$$

$$\mu = \pi \quad \text{when } F > F_c, \quad (3.283)$$

where

$$F_c \approx 0.9. \quad (3.284)$$

These findings are very similar to those obtained in (3.238)–(3.240) for the flow of Figure 3.47. Introducing the surface tension T on the surface SAS' of the bubble yields a discrete set of values of F for which $\mu = \pi/2$. A unique solution for which $F \approx 0.51$ is then obtained by taking the limit $T \rightarrow 0$ (see [170] for details).

The flow of Figure 3.70 is similar to that of Figure 3.69 except that the boundary of the wake is now approximated by two vertical lines, SJ and $S'J'$. This flow can be characterised by the Froude number

$$F = \frac{U}{gL}, \quad (3.285)$$

where L is defined in Figure 3.70. This is a crude model for the wake. It is, however, of mathematical interest because Joukovskii (see [69]) found an exact solution in the absence of surface tension. This solution is characterised by $F = (2\pi)^{-1/2}$. The results obtained for the flow of Figure 3.69 suggest by analogy that there is a solution for each value of F and that Joukovskii's solution is just a member of this family of solutions. This was confirmed by the numerical computations in [174], where it was shown that there is a solution for the flow configuration of Figure 3.70 for $0 < F < \infty$ satisfying (3.281)–(3.283), where μ is the angle between EA and AS in Figure 3.70 and where $F_c \approx 0.66$. As before a unique solution with $\mu = \pi/2$ can be selected by introducing surface tension and taking the limit $T \rightarrow 0$. Interestingly, the numerical computations suggest that the selected solution is Joukovskii's exact solution (see [174]).

The third example is a generalisation of the problem of a bubble rising in a tube considered in Sections 3.3.2 and 3.4.1. The flow configuration is shown in Figure 3.71(a). Gravity is acting vertically downwards. The angle between the left-hand wall and the horizontal is denoted by β , and the angle between the negative x -axis and the tangent line to the free surface JS at J is denoted by γ . When $\beta < \pi/2$, Figure 3.71(a) models a physical bubble rising in an inclined tube.

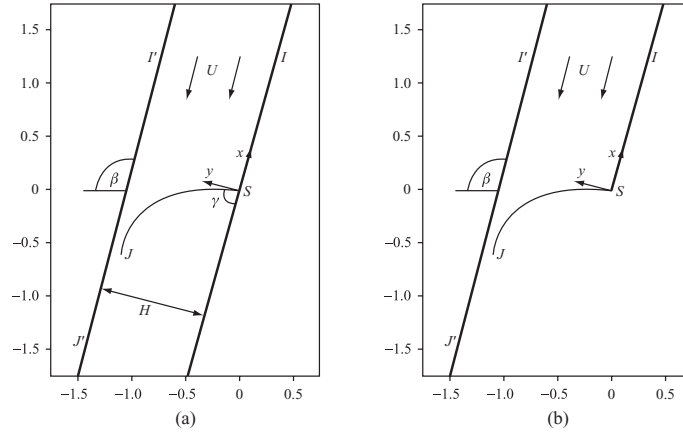


Fig. 3.71. The flow domain and the coordinates. This is a computed profile for $\beta = 7\pi/12$, $F = 0.11$ and $\omega = 10$.

This problem was studied experimentally by Maneri [107] and has been studied theoretically in [36] and [95]. The flow configuration of Figure 3.71(a) also describes a jet emerging from a nozzle and falling down along

a wall. In this case the flow is viewed as bounded on the left by an infinite wall and on the right by a semi-infinite wall and a free surface (see Figure 3.71(b)).

The flow can be characterised by the Froude number

$$F = \frac{U}{(gH)^{1/2}} \quad (3.286)$$

and the Weber number

$$\omega = \frac{\rho U^2 H}{T}. \quad (3.287)$$

Here ρ is the density of the fluid, U the velocity as $x \rightarrow \infty$ and H the width of the tube.

When $T = 0$ (i.e. $\omega = \infty$), the admissible values of γ depend on β and can be predicted by the local analysis of Section 3.3 (see Figure 3.38). When $0 < \beta < 2\pi/3$, there is a critical value F_c of the Froude number F such that solutions with $\gamma = 0$, $\gamma = \pi/3$ and $\gamma = \pi - \beta$ occur for $F > F_c$, $F = F_c$ and $F < F_c$ respectively. Values of F_c versus β are shown in Figure 3.72. However, for $2\pi/3 \leq \beta \leq \pi$ there is no such critical value of F , and $\gamma = 0$ for all $0 < F < \infty$ (see [95]).

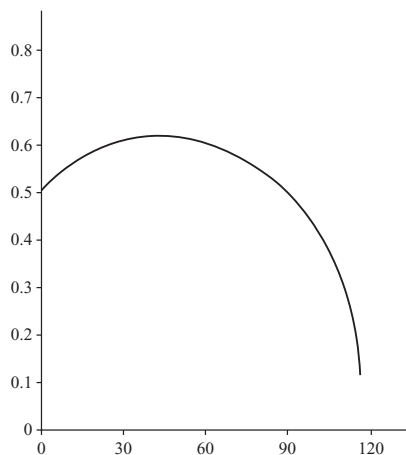


Fig. 3.72. Values of F_c versus β .

We note that these results include those of Section 3.3.2 as a particular case, since the flow of Figure 3.71(a) is simply half that of Figure 3.47. Figure 3.72 predicts $F_c \approx 0.506$. Dividing this value by $\sqrt{2}$ to take into account the different definitions of H in Figures 3.3.2 and 3.71(a) gives 0.36, in agreement with the value obtained in Section 3.3.2.

We now consider in more detail the problem of a bubble rising in an inclined tube (i.e. the flow of Figure 3.71(a)). The experimental data of Manieri [107] showed that for each value of $0 < \beta < \pi/2$, there is only one value of F for which a bubble exists. This does not agree with the numerical results, which predict a solution for each value of F and $0 < \beta < \pi/2$. This discrepancy can be removed by generalising the procedure described in Section 3.4.1. Thus again we introduce surface tension and take the limit as the surface tension tends to zero. Couët and Strumolo [36] chose for each value of β and ω the particular solution corresponding to the largest value of F for which $\gamma = \pi/2$. The selected results were found to be in good agreement with experiment.

The results in [95] summarised above show that the only possible values of γ when $T = 0$ are $\pi - \beta$, $\pi/3$ and 0 . Therefore there are no solutions with $\gamma = \pi/2$ when $T = 0$ unless $\beta = \pi/2$. This implies that the criterion, in [36] has to be used with T small but different from zero.

Here we follow [95] and use a different selection criterion, in which we take the limit $T \rightarrow 0$ instead of keeping $T \neq 0$ as in [36]. The numerical results in [95] show that for each value of $0 < \beta \leq \pi/2$ and ω there is a discrete set of values

$$F_i^*, \quad i = 1, 2, \dots, \quad (3.288)$$

where

$$F_1^* > F_2^* > F_3^* > \dots, \quad (3.289)$$

for which $\gamma = \pi - \beta$. This finding reduces to (3.259) when $\beta = \pi/2$. The numerical computations show that for a given value of i

$$F_i^* \rightarrow F^* \quad \text{as} \quad \omega \rightarrow \infty. \quad (3.290)$$

The selected values of F^* and the corresponding profiles are found to be in close agreement with the experimental data of Manieri [107] (see [95] for details). A typical selected profile for $\beta = \pi/3$ is shown in Figure 3.73.

3.4.4 Exponential asymptotics

Since the fingering problem of Section 3.4.2 has an exact solution when $T \neq 0$ (see (3.271), (3.272)), it is tempting to try to construct asymptotic solutions for T small in the form of a power series in T . This was achieved by McLean and Saffman [109], who showed that an arbitrary number of terms can be calculated. However, they found that this expansion leads to solutions for each value of $0 < \lambda < 1$. This is to be contrasted with the discrete set of solutions (3.278) found by direct numerical computation.

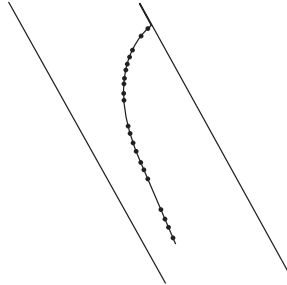


Fig. 3.73. Computed solution for $\beta = \pi/3$ and $F = F^* \approx 0.527$. The dots are the experimental values of Manieri [107].

This paradox was resolved by noting that the selection mechanism leading to (3.278) is associated with exponentially small terms in T . Such terms are smaller than any positive integer power of T as $T \rightarrow 0$ and therefore cannot be calculated by a power series in T . Exponential asymptotics has been used by many investigators to study this problem analytically (see Saffman [131] for a review and references).

Vanden-Broeck showed that the selection mechanism for a rising bubble that leads to (3.259) (see Section 3.4.1) is also associated with exponentially small terms.

Over the last 30 years, it has been found that exponentially small terms play a surprisingly significant part in free surface flow problems. We will encounter further examples later in this book. One example concerns the effect of surface tension on solitary waves (see Chapter 6). Other examples are the free surface flows generated by moving disturbances for small values of the Froude number or small values of the surface tension (see Chapter 8).